SCIENCE CHINA
Chemistry

•REVIEWS•
SPECIAL TOPIC: Electrocatalysis & Energy Science

November 2020 Vol.63 No.11: 1517–1542
https://doi.org/10.1007/s11426-020-9835-8

Advanced transition metal/nitrogen/carbon-based electrocatalysts for fuel cell applications

Tang Tang[1,2], Liang Ding[1,2], Zhe Jiang[1], Jin-Song Hu[1,2*] & Li-Jun Wan[1,2*]

[1]*Beijing National Laboratory for Molecular Sciences, CAS Key Laboratory of Molecular Nanostructure and Nanotechnology, Institute of Chemistry, Chinese Academy of Sciences, Beijing 100190, China;*
[2]*University of Chinese Academy of Sciences, Beijing 100049, China*

Received May 4, 2020; accepted July 20, 2020; published online October 19, 2020

The development of advanced transition metal/nitrogen/carbon-based (M/N/C) catalysts with high activity and extended durability for oxygen reduction reaction (ORR) is critical for platinum-group-metal (PGM) free fuel cells but still remains great challenging. In this review, we summarize the recent progress in two typical M/N/C catalysts (atomically dispersed metal-nitrogen-carbon (M-N-C) catalysts and carbon-supported metal nanoparticles with N-doped carbon shells (M@NC)) with an emphasis on their potential applications in fuel cells. Starting with understanding the active sites in these two types of catalysts, the representative innovative strategies for enhancing their intrinsic activity and increasing the density of these sites are systematically introduced. The synergistic effects of M-N-C and M@NC are subsequently discussed for those M/N/C catalysts combining both of them. To translate the material-level catalyst performance into high-performance devices, we also include the recent progress in engineering the porous structure and durability of M/N/C catalysts towards efficient performance in fuel cell devices. From the viewpoint of industrial applications, the scale-up cost-effective synthesis of M/N/C catalysts has been lastly briefed. With this knowledge, the challenges and perspectives in designing advanced M/N/C catalysts for potential PGM-free fuel cells are proposed.

electrocatalysis, ORR, metal-nitrogen-carbon, M@NC, fuel cells, oxygen reduction

Citation: Tang T, Ding L, Jiang Z, Hu JS, Wan LJ. Advanced transition metal/nitrogen/carbon-based electrocatalysts for fuel cell applications. *Sci China Chem*, 2020, 63: 1517–1542, https://doi.org/10.1007/s11426-020-9835-8

1 Introduction

As a clean energy conversion system, fuel cell converts the chemical energy of fuel into electric energy [1–3]. When hydrogen is used as the fuel, the device only generates water with zero carbon emission. Unlike thermal engines with the conversion efficiency of around 20% limited by the Carnot cycle [4], fuel cells are environmental-friendly with a theoretical efficiency close to 100% [5]. Stimulating by the rising need for electrical vehicles, proton-exchange membrane fuel cells (PEMFC) are recently reviving in both scientific and industrial communities. Although the overpotential for hydrogen oxidation reaction (HOR) at the anode is usually less than 20 mV, it is typically more than 300 mV for oxygen reduction reaction (ORR) at the cathode, even using the precious Pt catalyst [6]. Such an large cathode overpotential is closely related to the slow reaction kinetics of ORR, limiting the overall conversion efficiency of state-of-the-art PEMFC to about 45%–55% [7]. Therefore, the exploration of earth-abundant, highly efficient, and durable catalysts for ORR is essential for the commercialization of fuel cells.

Generally, the ORR takes place in two pathways: (1) 2-electron pathway and (2) 4-electron pathway, as illustrated in Figure 1 [8,9]. The former involves hydrogen peroxide in-

*Corresponding authors (email: hujs@iccas.ac.cn; wanlijun@iccas.ac.cn)

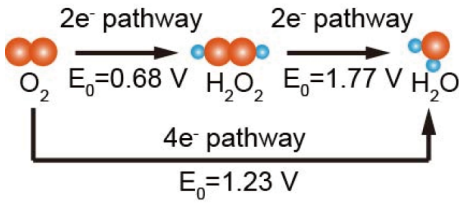

Figure 1 Illustration of 2-electron and 4-electron ORR pathways (color online).

termediate, causing detrimental influences on fuel cells. The oxygen molecule first adsorbs on the active site ($*O_2$) (Reaction (1.1)), followed by reacting with an electron and a proton to form H_2O_2 intermediate (Reaction (1.2)), which can be further reduced to H_2O, HO_2^- or OH^- (Reactions (1.3–1.5)).

2-Electron ($2e^-$) pathway:

$$O_2 \rightarrow *O_2 \quad (1.1)$$

$$*O_2 + 2e^- + 2H^+ \rightarrow H_2O_2 \quad (1.2)$$

$$H_2O_2 + 2e^- + 2H^+ \rightarrow 2H_2O \quad (1.3)$$

$$*O_2 + 2e^- + H_2O \rightarrow *HO_2^- + OH^- \quad (1.4)$$

$$HO_2^- + H_2O + 2e^- \rightarrow 3OH^- \quad (1.5)$$

In contrast, O_2 can be fully reduced to H_2O with no H_2O_2 intermediate in the 4-electron pathway. It not only is more efficient but also benefits the catalyst durability. In this pathway, after oxygen adsorbed on the active site, the $*O_2$ first reacts with one electron and one proton, generating *OOH intermediate (Reactions (2.1, 2.2). Two possible mechanisms are followed with the formation of two adsorbed *OH (Reaction (2.3)) or one adsorbed *O plus H_2O then *OH (Reactions (2.5, 2.6)). Subsequently, the adsorbed *OH further reacts with additional electron and proton to generate the H_2O product (Reactions (2.4, 2.7)). The rate-determining step (RDS) of ORR was the *OH desorption step [10].

4-Electron ($4e^-$) pathway:

$$O_2 \rightarrow *O_2 \quad (2.1)$$

$$*O_2 + e^- + H^+ \rightarrow *OOH \quad (2.2)$$

$$*OOH + e^- + H^+ \rightarrow *OH + *OH \quad (2.3)$$

$$2*OH + 2e^- + 2H^+ \rightarrow 2H_2O \quad (2.4)$$

$$*OOH + e^- + H^+ \rightarrow *O + H_2O \quad (2.5)$$

$$*O + e^- + H^+ \rightarrow *OH \quad (2.6)$$

$$*OH + e^- + H^+ \rightarrow H_2O \quad (2.7)$$

It is noted that both pathways involve multistep proton-coupled electron transfer, resulting in sluggish kinetics and thus high overpotentials. Developing efficient catalysts to lower such overpotentials and enhance $4e^-$ selectivity is urgent and has been investigated for decades. As mentioned above, the single-electron HOR is very efficient. A relatively low amount of precious Pt catalyst (about 0.05 mg cm^{-2}) at the anode can achieve desirable performance for fuel cells [2]. Similarly, Pt and its alloys are widely used as ORR catalysts, but a much higher loading of ~0.4 mg cm^{-2} is required to match the anodic HOR. Since Pt is a scarce and expensive metal, reducing its usage or eventually replacing it with non-precious materials would advance the development of fuel cells.

A large quantity of non-precious candidates have been developed as ORR catalysts working in either acidic or alkaline media over the past decades. Among them, the materials containing transition metal and nitrogen species on carbon supports (collectively noted as M/N/C) have attracted much attention and served in practical fuel cells due to their comparable ORR activity to commercial Pt/C catalysts. In 1964, Jasinski *et al*. [11] discovered that the metal phthalocyanines were active for ORR, initiating the research on this type of catalysts. Later on, it was found the pyrolysis of such metalloporphyrins increased the ORR catalytic activity and durability [12,13]. In 1989, Yeager *et al*. [14] found that heat-treating the mixtures of metal precursors, N-containing macromolecular polymers, and carbon supports achieved ORR catalysts with comparable performance to the pyrolyzed metalloporphyrin based catalysts. Since then, numerous heat-treated M/N/C catalysts sprung up.

Although great efforts have been made in developing new M/N/C materials with an emphasis on improving the ORR activity, the considerable challenges and issues still remained, including but not limited to the understanding of genuine active sites, the durability in the acidic electrolyte, and the controllable synthesis of well-defined active sites. The majority of M/N/C catalysts are prepared by the pyrolysis of source materials at high temperatures, leading to the complex catalyst structure with various potential active sites. N-doped carbon center, N, metal center coordinated with N, metal nanoparticles, *etc*., have been claimed as the active sites in various M/N/C catalysts. The influences of one active site on another are also vague and arguable. Some reports claimed that metal-free sites such as N-doped C or N itself could be as active as M-N sites or Pt especially in basic media [15,16], whereas it is generally found that incorporating metal could promote ORR activity and is necessary to achieve high ORR performance in acidic conditions [7]. Moreover, the performances of most reported M/N/C catalysts are still not sufficient for fuel cell applications. Due to the uncontrollable pyrolysis process, it is difficult to achieve a suitable catalyst structure with both high-density and intrinsically high-active sites. When assembling fuel cells, such insufficient intrinsic activity or density of catalytic sites has to be remedied by a thicker catalyst layer, compromising mass transfer and device performance. Fur-

thermore, the M/N/C catalysts are still suffering from severe degradation at high potential and thus poor durability [17]. The in-depth understandings of active sites and efforts in structural engineering and controllable synthesis are therefore required to achieve efficient and durable M/N/C catalysts.

Based on the structure of the active site, the heat-treated M/N/C catalysts can be classified into three types (Figure 2). The first is single-atom catalysts (SACs) with the structure of atomically dispersed metal-nitrogen-carbon (denoted as M-N-C), which is similar to metalloporphyrin molecules. In this case, M-N_x moieties are commonly considered as the ORR active sites. The second is carbon-supported metal nanoparticles encapsulated in N-doped carbon shells (denoted as M@NC), where metal and N co-activated carbon sites are generally proposed as the active center. Although the intrinsic activity of such site is normally slightly less than M-N_x site, it shows better durability in fuel cell operation since the metal nanoparticle is prevented from the direct corrosion from electrolyte and oxygen by carbon shell at applied potential, given that it is well graphitized and defect-less [18]. The third is the combination of the above two structures with the potential interaction therebetween.

In this review, we summarize the recent progress in M/N/C ORR electrocatalysts for fuel cell applications. Beginning with the brief introduction of synthetic methods to prepare M/N/C structure, the understandings of the activity origins of M-N-C and M@NC catalysts are first introduced in each structure, which will guide the exploration of advanced catalysts with improved ORR activity. The recently reported innovative strategies for enhancing the intrinsic activity and increasing the density of active sites are then summarized. Subsequently, the combination of M-N-C and M@NC sites to improve the ORR performance and the synergistic effects therebetween will be discussed [19,20]. Moreover, the fuel cell performance is affected not only by the intrinsic activity and the density of active sites, but also by the catalyst architecture. To translating material-level performance into high-performance and durable devices, we have discussed the recent progress in the structural engineering and durability improvement of the catalysts for high device performance and extended service life. Aiming at the practical application, we further brief the low-cost scalable production of M/N/C ORR electrocatalysts. With this knowledge, the perspective will be provided on the challenges and opportunities in designing advanced M/N/C materials as non-precious metal ORR catalysts for fuel cell applications.

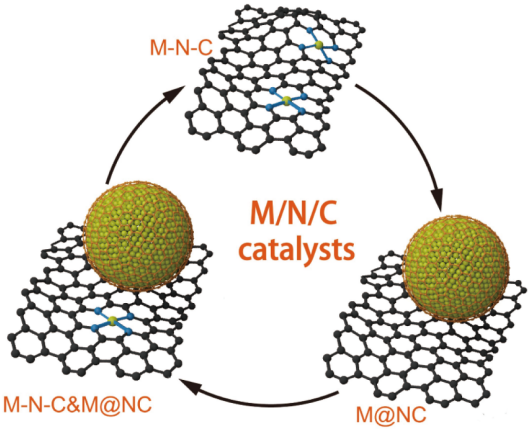

Figure 2 Schematic of three typical M/N/C catalysts: single-atomically dispersed M-N-C, metal nanoparticles wrapped in N-doped carbon shells (M@NC), and combined structure with both M-N-C and M@NC sites (M/N/C) (color online).

2 General synthetic methods for M/N/C catalysts

Since reported by Yeager *et al*. [13] in 1989, the pyrolysis of mixtures containing metal source (typically Fe, Co, Mn), N, and C species has become the common synthetic methods for M/N/C structure. In general (Figure 3(a)), the mixed precursors containing metal source (*i.e.*, adsorbed metal salt, and metal oxides), N species (*i.e.*, N-rich ligand, and N-rich polymer), and carbon supports (*i.e.*, graphene, carbon nanotubes (CNTs), and porous carbon) are thermally treated at high temperature (~600–1200 °C) in inert environments such as Ar or N_2 atmosphere [2,7]. Such processing commonly produced metal nanoparticles, metal-nitrogen coordinated sites (M-N_x), and nitrogen-doped carbon sites (N-C).

Based on the clustering degree, the metal components exist in the catalysts in form of nanoparticle (>5 nm), cluster (0.1–5 nm), or single-atomic state. The size reduction benefits the utilization of active atoms and the increase of active sites [21]. Ultimately, downsizing metal components into single-atomic scale gives the well-defined structure of active sites with maximal atomic utilization [22], leading to enhanced reaction selectivity and activity. However, the clustering degree of atoms in the catalysts varies significantly from one to another. To better control the pyrolysis process and metal clustering, some well-defined molecular precursors homogeneously containing the above species, including metalloporphyrins and metal-organic-frameworks (MOFs), have been intensively used [23]. Due to the highly reactive nature of transition metal, the products usually require additional acid washing to remove the aggregated metal particles. The second pyrolysis is subsequently carried out under inert environments to remedy the graphitic structure and M-N_x structure or under N-rich environment to increase N doping concentration. Although the last two steps can improve the electrocatalytic activity and stability of the products it usually leads to the decrease of active species (commonly lower than 5 wt% for single-atomic M-N-C structure or 15 wt% for M@NC structure).

In most cases, M@NC structure can be obtained by in-

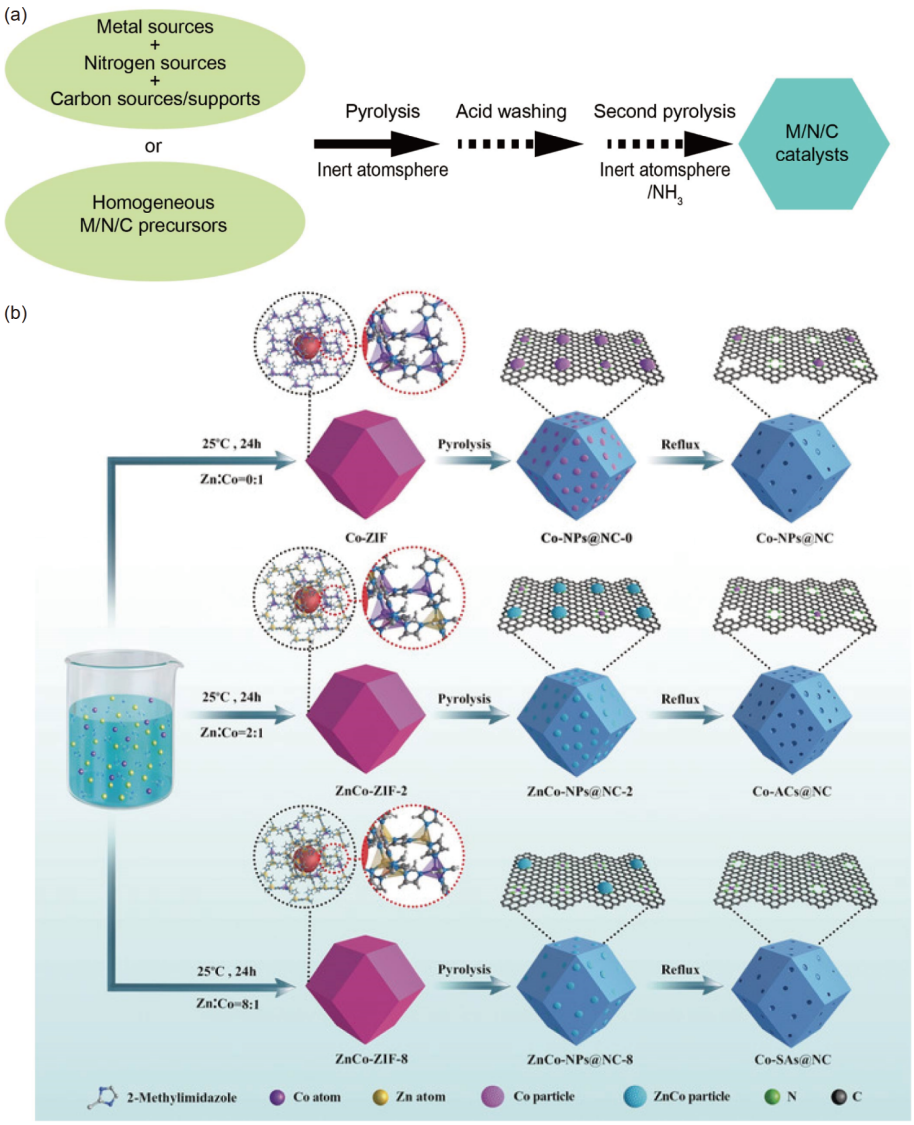

Figure 3 (a) Schematic of the typical synthesis route for M/N/C catalysts; (b) schematic of the preparation of MOF-derived Co catalysts. Adapted with permission from Ref. [26], Copyright by Wiley (color online).

creasing the metal loading in precursors, while the preparation of single-atomic M-N-C structure requires the delicate control of metal loading and distribution. To achieve the high-loading M-N-C structure, the additional procedures are normally required to prevent the metal aggregation. We have reported a cascade protection strategy to prepare a variety of high-density M-N-C structures by sequentially isolating and anchoring active species on substrate (discussed later) [24]. For homogeneous precursors such as MOFs, physical steric hindrance is commonly used to prevent the agglomeration of active metal species during pyrolysis [25]. For instance, by tuning the content of volatile Zn in ZnCo ZIF-67 precursors (Figure 3(b)), Deng *et al.* [26] realized the controllable synthesis from M@NC, metal clusters, and Co single-atom on carbon support.

Generally, the catalyst activity is mainly determined by the intrinsic activity and the density of exposed catalytic sites. Tremendous researches are devoted to enhancing the intrinsic activity through regulating the electronic structure of active sites while the density of active sites can be improved through morphological and structural engineering. However, the charge transport is another important factor that affects the catalytic performance of a catalyst. The electrical conductivities of M/N/C catalysts significantly depend on the graphitization of carbon supports. It is found that the use of precursors with highly conjugated units such as polyaniline, and polypyrrole can improve the electrical conductivities of the derived carbon materials [18]. The conductivity can also be significantly improved by elevating the temperature of thermal treatment or carrying out secondary heat treatment. Moreover, the high dosage of metal components is favourable for the increase of electrical conductivity of carbon

matrix *via* catalytic graphitization at high temperatures [27,28]. For MOF-derived materials, combining with additional highly-conductive substrates such as graphene and carbon nanotubes (CNTs) can further improve their electrical conductivity [29]. These results indicate that the catalyst structure can be regulated through precisely controlling the synthetic strategies, offering possibilities to enhance its catalytic performance.

3 Atomically dispersed M-N-C electrocatalysts

Metalloporphyrin molecules are typical M-N-C structures with well-defined atomically dispersed active sites. However, their high cost, non-scalable synthesis, and insufficient ORR activity as well as poor durability hinder them from practical use. Although the heat treatment of metalloporphyrins can enhance their ORR activity [12], the complexity of the derived M/N/C catalysts brings up substantial challenges for identifying the real ORR active sites [30] and the cost issue still remains. Numerous efforts have been devoted to circumventing this issue by developing catalysts with analogous active sites *via* cost-effective approaches. A variety of strategies such as polymer pyrolysis, spatial isolation, and hard templates have been explored to synthesize different atomically dispersed M-N-C structures with varied M-N_x coordination. It is found that the rational design of the precursors at the atomic level is crucial for achieving well-defined M-N_x coordination and increasing the density of active sites but still remains a great challenge. By virtue of the unique structure and coordination, MOFs have emerged as promising precursors for the synthesis of M-N-C SACs. Some of them have shown promising ORR performance. For example, Fe-N-C SACs with atomically-dispersed Fe-N_4 moieties have been demonstrated with ORR activity approaching that of Pt in acidic electrolyte [31]. Based on these strategies, the SACs with multiple-atom-coordination sites have also been explored, such as sulfur and phosphorus-codoped M-N(S,P)-C [32,33] and bimetal M_1,M_2-N-C [34,35].

Notably, although the tremendous publications have claimed their products as single-atomic catalysts, a substantial portion of catalysts should contain both single-atomic metal centers and metal clusters. The intensive characterizations *via* advanced techniques such as extended X-ray absorption fine structure (EXAFS) and X-ray absorption near edge structure (XANES) together with in-depth analyses are required to rule out metal-metal coordination in such catalysts.

3.1 Active sites in M-N-C structure

The goal of ORR catalysts is to achieve high selectivity ($4e^-$ pathway to H_2O *vs*. $2e^-$ pathway to H_2O_2) and fast reaction rates at the potentials as close as the thermodynamic value (1.23 V). Identifying the location and structure of the most active site is critical for understanding the activity-structure relationship and guiding the rational design and controllable synthesis of catalysts with well-defined highly-active sites for improving catalytic performance. Hampered by the complex active sites, however, the genuine active sites in M/N/C electrocatalysts are still arguable over the decades of study. Recently, the developing fabrication of M-N-C SACs provides opportunities for tackling this puzzle.

Transition metal (iron, cobalt, manganese, or copper, *etc*.) complexes with planar N_4-macrocycles such as porphyrins and phthalocyanines have been known as molecular catalysts to facilitate ORR for a long time [36–38]. They have been used in both electrocatalytic systems and thermal/chemical catalytic systems [39]. Since Jasinski *et al*. [11] found that the metalloporphyrins exhibited ORR performance in the aqueous heterogeneous electrocatalytic system in 1964, extensive studies on M-N_4 macrocycle electrocatalysts for ORR have been performed. Taking iron porphyrins as examples (Figure 4(a)), the Fe-N_4 structure is usually identified as the active site [40]. The basic mechanism starts with oxygen adsorption and binding in concert with electron transfer on a metal center, whereby oxygen is formally reduced and metal center is formally oxidized. The adsorbed higher energy intermediates are stabilized by the metal center

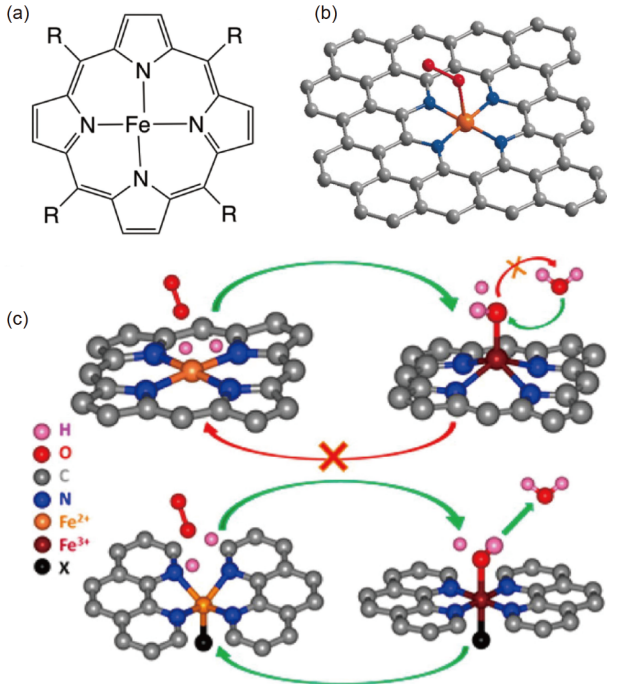

Figure 4 (a) Molecular structure of typical iron porphyrins. (b) Schematic model of single-atom Fe-N-C structure. Fe (orange), N (blue), O (red), C (gray). Adapted with permission from Ref. [42], Copyright by Wiley. (c) Illustration of the structural transformation of Fe-N upon O_2 exposure. Adapted with permission from Ref. [45], Copyright by the American Chemical Society (color online).

and further react along the paths from O_2 to H_2O or H_2O_2.

Similar to homogeneous systems, the ORR in heterogeneous systems is also influenced by the coordination environment of catalytic sites. For example, Zuo's group [41] probed the effects of Fe coordination. They investigated the ORR behavior of 4- and 5-coordinate FePcs attached to CNTs through EXAFS and XANES. It was found that the addition of a fifth ligand on the Fe center to form the square-planar geometry significantly enhanced the ORR activity in acid.

The metal center in atomic dispersion has commonly to be stabilized by coordinating with other atoms on support. N-coordination in M-N-C SACs not only offers M-N_x as ORR active sites but also effectively stabilizes the atomically dispersed metal centers, preventing them from aggregation even under high-temperature pyrolysis. For example, Li's group [42] reported a catalyst of isolated single-atom Fe/N-doped porous carbon (ISA Fe/CN) with a half-wave potential ($E_{1/2}$) of 0.90 V, outperforming the commercial Pt/C. EXAFS and XANES analyses confirmed the existence of the Fe-N_4 active site, as illustrated in Figure 4(b). Recently, more evidence including density functional theory (DFT) calculations and Möβbauer spectroscopy suggested that Fe-N_x moieties should be the most active sites in M-N-C SACs [43,44]. Mukerjee's group [45] applied *in-situ* XANES measurements to identify the transformation of Fe-N structure upon O_2 exposure. As displayed in Figure 4(c), the Fe(II)/(III) redox couple in Fe-N_x center was ascribed to be responsible for the observed ORR activity. The original Fe(II) species featured the out-of-plane displacement. Upon O_2 binding to Fe center, the Fe(II) species were oxidized to Fe(III) and moved back toward the N_x-C plane. This observation directly suggested that Fe-N_x sites should be the ORR active sites. It was proposed that the appropriate adsorption energies of O_2 and intermediates on M-N_x decreased the free energy for successive steps, thus resulting in excellent electrocatalytic activity for ORR.

3.2 Strategies to enhance the intrinsic activity of M-N-C structure

The electronic structure of the active site determines the energy barriers for the adsorption/desorption of the reaction intermediates. Therefore, the intrinsic ORR activity of the M-N-C structure can be modulated by modifying the electronic structure of the metal center to regulate the chemical adsorption energy of oxygen-containing intermediates. It can be done by precisely tuning the coordination, chemical bonding, and chemical environments of the metal center, as exemplified below.

3.2.1 *Heteroatom coordination*

In the homogeneous catalytic system, adjusting the coordination environment of molecular metal-macrocycle complexes by changing ligands is a common strategy to enhance ORR performance [37]. Alternatively, introducing heteroatoms such as B, P, or S with a discrepancy in electron spin density and electronegativity into the M-N_x coordination structure of the pyrolyzed M-N-C catalysts can induce changes in charge distribution, affecting the adsorption of oxygen-containing intermediates, thus the catalytic activity [46–49]. However, during the pyrolysis process, which was commonly applied to prepare M-N-C catalysts, doping heteroatoms in M-N_x structure in a well-defined way remains challenging. Chen's group [50] recently developed nitrogen and phosphorus dual-coordinated Fe active site (Fe-N/P-C) (Figure 5(a)). It exhibited excellent ORR activity with an $E_{1/2}$ of 0.867 V. Experimental and theoretical results suggested that the configuration of N/P dual-coordinated Fe active site was favorable for the adsorption/desorption of oxygen intermediates, thus accelerating the ORR reaction kinetics. Mu's group [48] (Figure 5(b)) reported that the introduction of B into the Co-N_x site gave an electron-deficient site. It could activate the electron transfer around it, strengthening the interaction with oxygenated species and thus accelerating $4e^-$ pathway reaction kinetics during ORR.

3.2.2 *Peripheral electronic modulation*

According to previous reports, the size of the carbon plane greatly influenced the kinetic activity of the accommodated Fe-N_4 site [51]. This can be attributed to the interaction between the delocalized π-bond of the carbon plane and the d-orbital of Fe center in Fe-N_4 coordination. The large carbon plane containing electron-rich π-bond with a higher degree of delocalization increased the d-orbital energy level of the Fe-N_4 sites, resulting in stronger adsorption of ORR intermediates on Fe-N_4 site [52]. Lee's group [53] reported a versatile strategy to enhance the ORR activity of Fe-N_4 sites by tuning the electron-withdrawing/donating properties of the carbon plane by incorporating various sulfur functionalities (Figure 6). The experimental results and theoretical calculations elucidated the electron-withdrawing/donating functionalities effect. The d-band center of Fe was lowered by introducing the oxidized sulfur as an electron-withdrawing functional group. It reduced the intermediate adsorption energy on the Fe-N_4 site, thus facilitating the ORR.

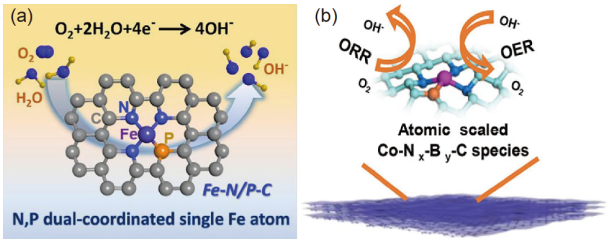

Figure 5 Schematic of P-doped Fe-N-C (a) and B-doped Co-N-C (b) structures. Adapted with permission from Refs. [50], and [48], Copyright by the American Chemical Society, respectively (color online).

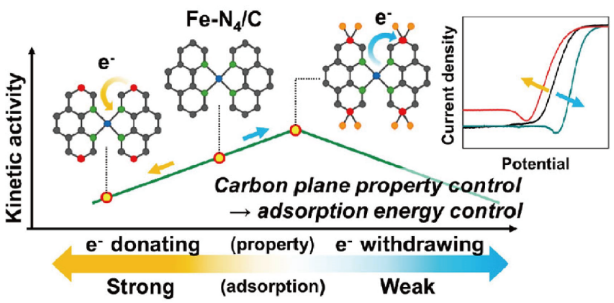

Figure 6 Schematic of peripheral electronic modulation by electron-withdrawing/donating groups. Adapted with permission from Ref. [53], Copyright by the American Chemical Society (color online).

Moreover, other heteroatoms with higher electronegativity such as Cl^- and O^{2-} were also capable of constructing such an electron-withdrawing environment around the Fe-N_4 site [52,54].

3.2.3 *Multimetal-center modulation*

It was further discovered that the performance of M-N-C catalysts followed the Sabatier principle. The proper M-O binding energy contributed to the desired catalytic behavior at the top of the volcano-shape curve [55,56]. Although Fe-N_4 active center located at a considerably high position on the M-O strong binding leg and exhibited excellent catalytic performance, it still carried considerable disparity to the optimal binding energy. It is thus desirable to regulate the configuration of active centers toward optimal adsorption-desorption behavior of oxygen species. Recent reports demonstrated that introducing additional metal into the M-N-C site to form the multinuclear M_1M_2-N-C site would be effective for modulating the M-O binding energy. For example, Xing's group [35] constructed a bimetal Fe-Co active center. The Fe coordinated with the Co-N_x site to bond another OH ligand, forming a new site with the weakened adsorption energy to the intermediates. DFT calculations confirmed that the OH ligand on such a bi-nuclear site was much stable in the whole range of ORR potential. As evidenced by both DFT calculations and XANES spectroscopy, the achieved $FeCoN_5$-OH site positively shifted to the apex of the volcano (Figure 7) and thus resulted in better ORR performance. Wu *et al.* [34] also reported a (Fe, Co)-N-C bimetal site, exhibiting comparable performance to Pt/C in the acidic electrolyte with an $E_{1/2}$ of 0.863 V. Fuel cell measurements demonstrated that such bimetal sites were very stable during the device operation. These strategies suggested that the construction of a multi-metal center might be an option for optimizing the electronic structure of the M-N-C site to accelerate ORR.

3.3 Strategies to increase the active site density of M-N-C structure

The ORR performance of a catalyst is determined by both the intrinsic activity of each active site and the number of effective active sites. The low-density active sites lead to the mass/charge transfer issues when used in fuel cells [57]. Due to the uncontrollable and complicated reactions during heat treatment, the desired structure usually cannot be achieved through simply increasing the dosage of metal precursors. Rational designs are thus needed to improve metal dispersion and prevent single-atomic metal centers from aggregation at high loading. Therefore, precise control of catalyst precursors and their evolution at the molecular level may be effective for achieving high-density M-N-C SACs [7,22,27,58].

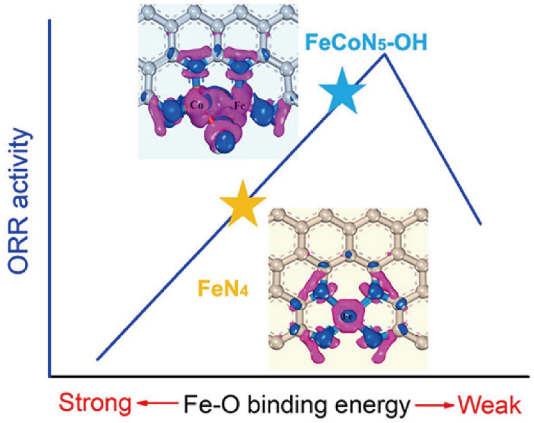

Figure 7 Schematic volcano curve of Fe-O binding energy and ORR activity for FeN_4 and $FeCoN_5$-OH active sites. Adapted with permission from Ref. [35], Copyright by the American Chemical Society (color online).

3.3.1 *MOF-based spatial isolation strategy*

Benefiting from the unique elemental distribution and the covalent bonds of metal atom, N, and C, MOFs have emerged as promising precursors for preparing M-N-C catalysts. For example, Chen's group [59] developed a strategy using ZIF-8 to host additional Fe as the precursor to prepare catalyst, achieving attractive ORR performance. Unfortunately, the catalyst structure was still in poor control. To figure this out, doping active metal such as Fe or Co into ZIF-8 structure during the synthesis would be able to deliver more uniformly dispersed and high-density M-N_x active sites in 3D carbonized frameworks. Li's group [25] recently developed a MOF-confined pyrolysis strategy to fabricate high-density Co-N-C SACs. As displayed in Figure 8(a), Zn^{2+} ions in MOF structure played an important role in separating Co^{2+} ions. During the pyrolysis, Zn species were evaporated out to create a highly porous structure, while Co atoms were anchored by N species, forming the isolated Co-N-C active sites. The overall morphology of the original ZIF-8 remained well (Figure 8(b, c)) after the pyrolysis. The isolated Co atoms were directly observed by the high-angle annular dark-field scanning transmission electron microscopy (HAADF-STEM) (Figure 8(d, e)). With this strategy,

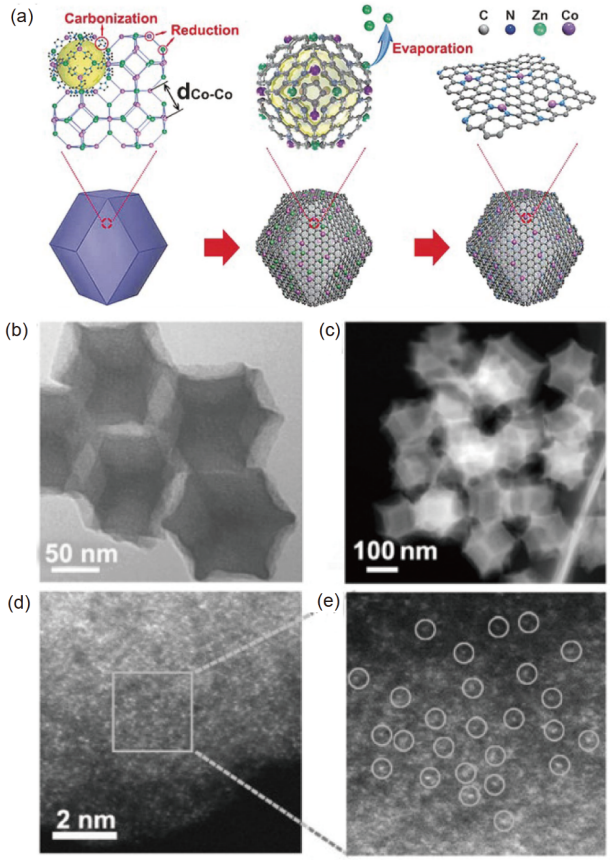

Figure 8 (a) Schematic formation of Co-N-C SAC *via* MOF precursor; (b–e) TEM and HAADF-STEM images, showing the catalyst morphology and single-atomically dispersed Co. Adapted with permission from Ref. [25], Copyright by Wiley (color online).

the Co loading was up to 4 wt%, higher than that in the catalysts prepared through physically mixing precursors. The achieved Co-N-C exhibited a high ORR activity with an $E_{1/2}$ of 0.881 V. Similar idea could be also seen in the work reported by Wang *et al*. [60]. They found that using 5% Zn in the MOF precursor achieved high-density Co-N-C SAC, delivering a high $E_{1/2}$ of 0.9 V in 0.1 M KOH solution.

3.3.2 *Gas-transport/migration approach*

Conventional chemical routes to fabricate atomically dispersed M-N-C usually involve multiple synthetic steps, including solution-based dispersion and separation, the adsorption and reduction of metal precursors. Due to the insufficient interaction between active single atoms and substrate under a high reaction temperature, metal atoms easily aggregated into large particles. Wu's group [61] demonstrated a unique gas-migration strategy for directly transforming bulk transition metals such as Cu, Co, and Ni into the corresponding atomically-dispersed metal-N_x species with the assistance of NH_3. As shown in Figure 9, the pyrolyzed ZIF-8 with empty zinc nodes and abundant defect sites acted as an ideal host for coming metal atoms. Simultaneously, ammonia molecules hauled the surface atoms out of Cu foam, forming volatile $Cu(NH_3)_x$ species. These species were transported *via* carrier gas and then trapped by the defects in N-rich pyrolyzed ZIF-8 support, generating the isolated Cu-N-C SACs. The Cu loading was reported to be 0.54 at%. The resulted Cu-N-C SAC exhibited excellent ORR performance in terms of an $E_{1/2}$ of 0.895 V. To avoid the corrosive NH_3 gas, they further used Cu_2O as the metal source and developed N-rich carbon support to trap the volatile metal species, which also achieved the atomically dispersed metal-N_x species [62]. Such an ameliorated gas-phase strategy delivered a Cu loading up to 0.45 at%. The catalyst demonstrated an $E_{1/2}$ of 0.92 V for ORR. Moreover, Mo and Sn-based M-N_x structures have also been prepared through a similar approach, indicating its versatility in the synthesis of M-N-C catalysts.

3.3.3 *Hard-template strategy*

The synthesis of M-N-C catalysts generally involves the step of high-temperature pyrolysis to achieve the coordination of M-N_x and guarantee sufficient conductivity and stability. However, metal atoms tend to form large metal particles under high temperature, causing the loss of active component. This not only requires additional treatments such as post-acid-etching and heat treatments but also leads to the low loading of active M-N_x sites. Hard templates have been suggested to prevent the metal aggregate and promote the formation of pores. SiO_2, which can be removed *via* KOH or HF, has been widely utilized as one of such hard templates [63]. For example, Monteverde Videla *et al*. [64] demonstrated the silica templates in a pyrolyzed FePc system, achieving the more uniform Fe distribution in micropores and thus the increased activity and better $4e^-$ reduction process. Joo's group [65] recently applied a silica coating with adsorbed iron porphyrins onto CNTs. Such a coating

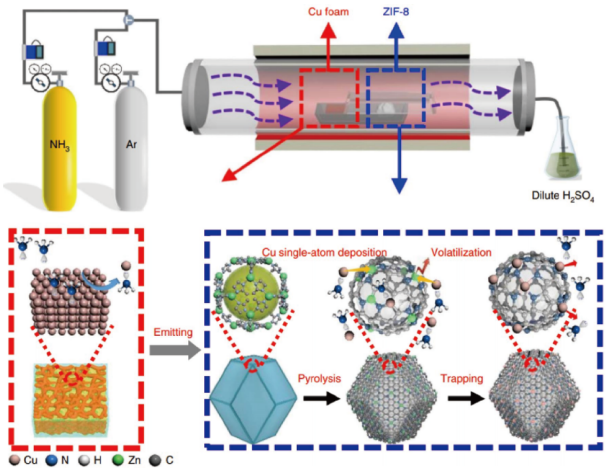

Figure 9 Schematic preparation of Cu-N-C SAC through solid-state gas transporting strategy. Adapted with permission from Ref. [61], Copyright by Nature publication group (color online).

could confine the precursors during pyrolysis and prevent Fe aggregation to achieve high-density Fe-N_x sites. Temperature-controlled *in-situ* X-ray absorption spectroscopy (XAS) suggested that the interaction of silica layers with Fe-N_4 moieties contributed to the formation of catalytically active Fe-N_4 moieties during high-temperature pyrolysis (Figure 10). The Fe loading was up to 2.9 wt% through this strategy. The resulting catalysts showed improved ORR activity in alkaline media with an $E_{1/2}$ of 0.88 V as well as excellent durability. Besides, hard templates derived from other materials such as ZnO and V_2O_5 have also been demonstrated to synthesize Fe-N-CNT, Co-N-GC, Fe/N/S-C, and FeCoPc-C as well, respectively [66–69].

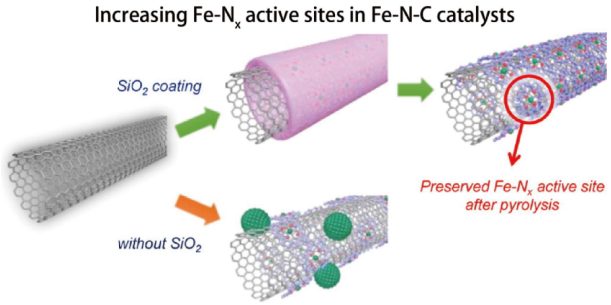

Figure 10 Schematic synthesis of Fe-N-C on CNTs *via* silica hard template. Adapted with permission from Ref. [65], Copyright by the American Chemical Society (color online).

3.3.4 *Molecular-level cascade anchoring strategy*

Although a great number of attempts have been made to increase the density of single-atomically dispersed M-N-C sites in catalysts, it is still challenging to prevent the aggregation of reactive metal atoms at high-temperature processing for the formation of M-N_x coordination, especially under the high-dosage condition. Few reports can achieve the metal loading of over 5 wt%. Special attention should be paid to the isolation and securing of metal atoms during the synthesis.

We recently developed a facile, low-cost, and scalable strategy to produce high-density M-N-C SACs [24] by cascaded anchoring and securing metal ions/atoms. As illustrated in Figure 11(a), each metal ion was firstly sequestered with low-cost and hydroxyl-gorup-rich glucose (chelating agent), and then effectively secured onto the oxygen-species-

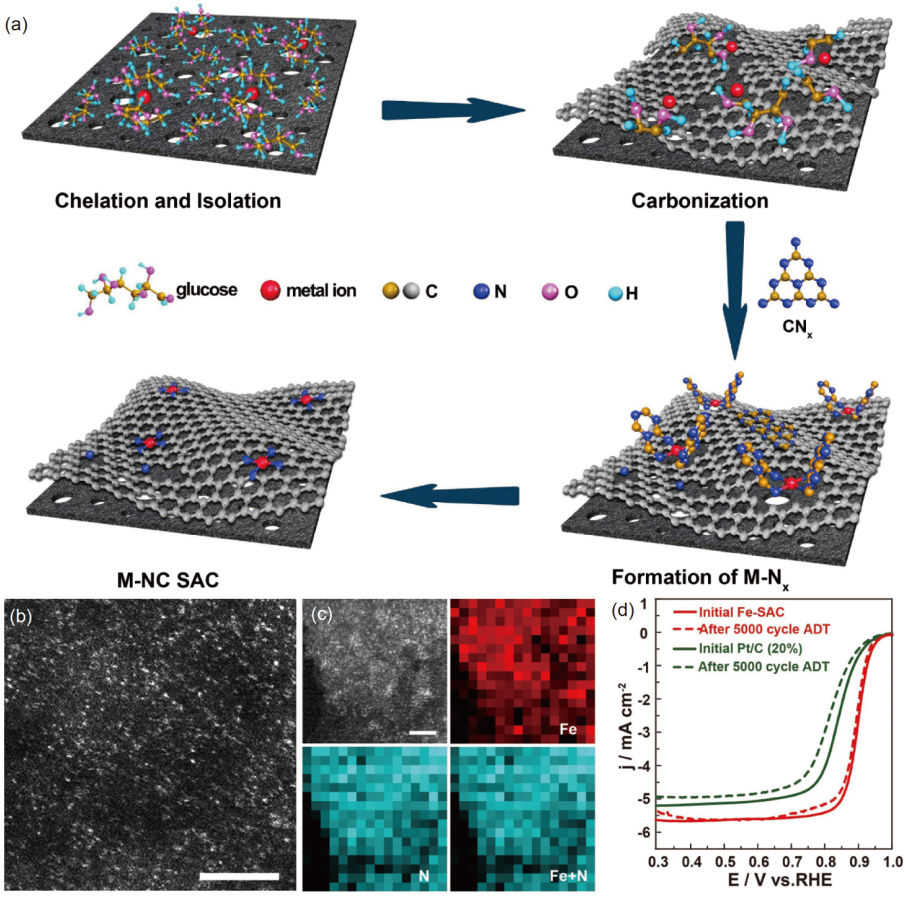

Figure 11 (a) Schematic of the cascade anchoring strategy for the general synthesis of M-NC SACs; (b) HAADF-STEM image, (c) corresponding EELS mapping, and (d) ORR polarization curves of Fe-NC SAC. Adapted with permission from Ref. [24], Copyright by Nature publication group (color online).

rich surface of nanoporous carbon substrate *via* the interaction of hydroxyl group and substrate. The high surface area of the porous substrate enabled the high loading of the metal-glucose complex. The much excessive glucose (relative to metal ions) in the precursor solution guaranteed that the metal complexes were physically isolated by glucose molecules in spatially uniform distribution on the entire accessible surface of the substrate. During initial pyrolysis (<~500 °C), the decomposed residues could still keep isolated in this case. As the temperature further went up, the N-species, CN_x from the decomposition of melamine, came in and bounded with the released metal ions to form M-N-C sites, simultaneously anchoring them onto carbon substrate and taking over the protection of metal atoms from aggregation. Through such a cascade anchoring strategy, the high-loading of M-N-C SACs were successfully achieved. For example, the metal loading in Fe-N-C SAC was 8.9 wt%. The HAADF-STEM images, EXAFS analyses, and corresponding electron energy loss spectroscopy (EELS) confidently evidenced that the high-density Fe-N_x species existed on the substrate in single-atomic dispersion (Figure 11(b, c)). Benefiting from the high-density active sites, the Fe-N-C SACs demonstrated superior ORR performance in terms of an $E_{1/2}$ of 0.9 V (Figure 11(d)) and remarkable stability.

Based on the principles of coordination chemistry, a wide range of chelating agents, metal precursors, and N sources could be selected in this cascade processing, making it a versatile strategy for the synthesis of a variety of M-N-C SACs with a high meal loading. Besides Fe-N-C SAC, Mn-, Co-, Ni-, Cu-, Mo-, Pt-N-C SACs, *etc*. have been demonstrated with a metal loading of up to 12.1 wt% (Figure 12(a–f)). Since the whole process is very simple and easy to scale up (basically, dissolution, drying, and pyrolysis), this strategy enabled the low-cost mass production of M-N-C SACs, attractive for various industrial applications.

Later on, Zhang's group [70] reported a similar strategy by using 1,10-phenanthroline as both chelating agent and N sources to synthesize Ni-N-C SACs on a commercial carbon substrate. The high-performance catalysts with a metal loading of 5.3 wt% were obtained. The relatively lower metal loading could be due to the much less solubility of phenanthroline than glucose.

4 M@NC electrocatalysts

Besides the atomically dispersed M-N-C electrocatalysts with M-N_x moieties as the active sites, metal-based nanoparticle wrapped by M@NC stands for another type of active site with considerable ORR performance. Such metallic or metal carbide nanoparticle-related sites are generally formed by the aggregation of metal atoms during pyrolysis and protected by graphitic carbon layers. Rojas' group [71] compared the ORR activity and poisoning behavior of the graphene and the catalysts derived by the calcination of FePc in basic solution. It was found that the poisoning has less effect on the calcinated Fe@NC catalyst than FePc itself. Although the Fe-N_x species exhibited the highest activity while the derived Fe@NC also showed considerable ORR performance which is much higher than metal-free sites.

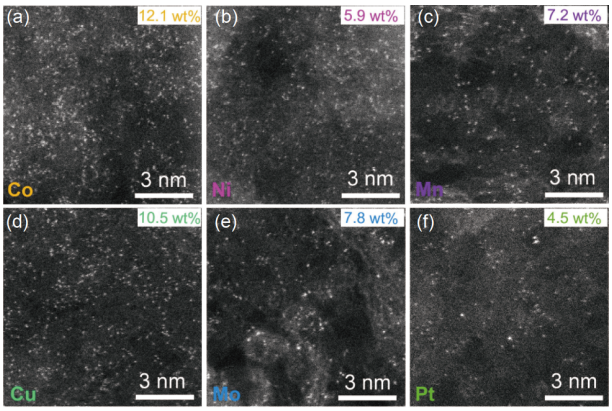

Figure 12 HAADF-STEM images of Co SAC (a), Ni SAC (b), Mn SAC (c), Cu SAC (d), Mo SAC (e), and Pt SAC (f). Adapted with permission from Ref. [24], Copyright by Nature publication group (color online).

Our group [72] has reported a nanocable-like catalyst where the core was carbon nanotube and the shell was iron carbide nanoparticles encapsulated in N-doped (Fe_3C@NC). By sequentially coating Fe_3O_4 layer as iron precursors onto CNT cores and then polydopamine layer as N-doped carbon source and reductant, the reduced iron carbide nanoparticles could be well confined in the N-doped carbon shell and prevented from aggregation during the pyrolysis. Systematic experiments showed that the synergy between the encapsulated Fe_3C nanocrystals and the porous NC shells significantly enhanced the catalytic performance for ORR.

For this kind of M/N/C catalyst, metal nanoparticles are encased by N-doped carbon shells and thus segregated from the corrosive acidic or basic electrolyte. Although they commonly show relatively lower intrinsic ORR activity than M-N_x active sites, the well-protected inner metal cores can survive during the hash cycling condition of fuel cell operation, giving it much better device durability than the single-atomic M-N-C materials, which normally suffers from insufficient stability due to the metal site dissolution. Exploration of M@NC materials could thus promote the application of non-precious M/N/C catalysts in practical fuel cells. The challenges remain in the fabrication of well-defined and high-density M@NC sites with defect-less graphitic carbon shells.

4.1 Active sites in M@NC structure

By means of *in-situ* XANES and EXAFS spectroscopy,

Mukerjee's group [73] comparatively studied the ORR performance of two different M/N/C catalysts with or without Fe-N_x coordination. It was found that the presence of both Fe-N_x species and Fe nanoparticles embedded in carbon supports contributed to the high ORR activity in acidic media, indicating Fe@NC site was also active for ORR.

Bao's group [74] synthesized a peapod-like carbon nanotube catalyst. Fe nanoparticles protected by several N-carbon layers were incorporated inside carbon nanotube or N-doped carbon nanotube, segregating from the corrosive environment outside. Such a structure exhibited significantly higher acidic ORR performance than bare nanotubes as well as a very steady performance in PEMFC operation. Using DFT calculation, the authors proved the effective electron transfer from the encapsulated Fe nanoparticles to the outer carbon nanotubes. As displayed in Figure 13, the models containing a Fe_4 nanoparticle inside N-doped (6,6) single-wall CNT or pure CNT were constructed. It was found that both Fe nanoparticle and N-doping facilitated the O_2 adsorption. The electron transfer from nanoparticle to nanotube shell decreased the local work function of surface carbon. With the N-doping in carbon lattice, the electron density state of carbon was further increased to near Fermi level, benefiting the adsorption of O_2 and intermediates. As a result, such Fe@NC structure could act as a highly-active ORR site.

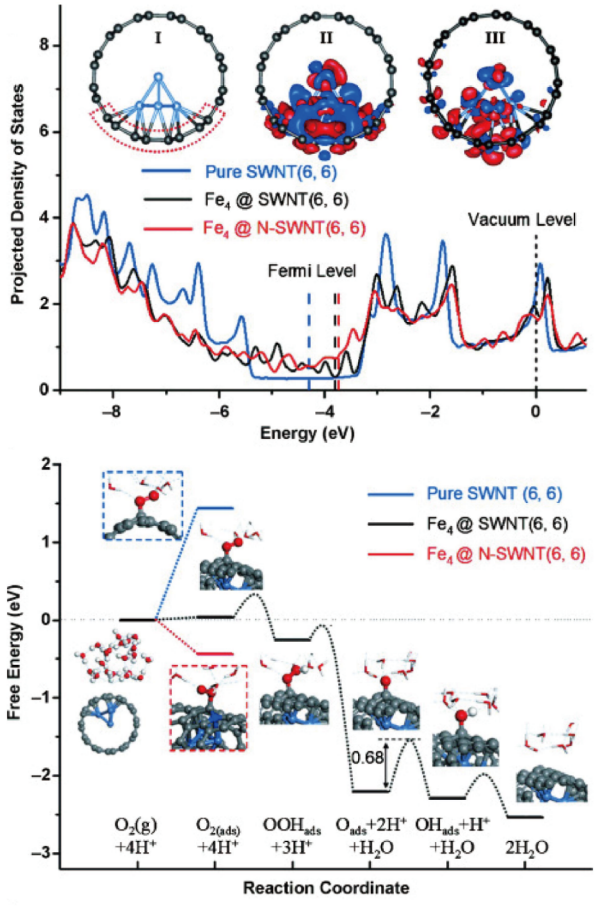

Figure 13 DFT calculations of SWNT, Fe_4@ SWNT, and Fe_4@N-SWNT models. Adapted with permission from Ref. [74], Copyright by Wiley (color online).

4.2 Strategies to enhance the intrinsic activity of M@NC

4.2.1 Metal core engineering

For M@NC structure, the electronic modulation on the interaction between the inner metal core and outer N-carbon shell has great effects on its electrocatalytic performance. Xing's group [75] developed a unique two-stage encapsulation strategy (Figure 14(a)) to acquire Ni@NC_x, Fe@NC_x, and NiFe@NC_x. Fe, Ni-containing MOFs were employed as metal hosts at low temperature, while the melamine was adopted as both N source and soft template at high temperature. The flexible MOF template allowed the easy adjustment of the metal ratio in the bimetallic core. XPS results indicated the NiFe alloy led to the favorable electronic structure of outer carbon layers, giving NiFe@NC_x the best ORR performance (Figure 14(b)). It was concluded that the bimetal NiFe core affected the ORR activity of outer N-doped carbon to a larger extent (Figure 14(c)). Similarly, Chen's group [76] reported that the incorporation of Ni to fabricate the Fe_xNi-FeO_y-NC triphase heterointerface appreciably enhanced the intrinsic catalytic activity for ORR by shifting the electronic structure of FeO_y. These findings pave new ways to rationally design high-performance M@NC catalysts.

4.2.2 Carbon shell engineering

It has been widely demonstrated that the concentration and configuration of N species in the outer carbon shell of M@NC structure play crucial roles in modulating its electronic structure and thus catalytic performance [77]. The N species usually exist in four configurations in carbon plane: pyridinic N, pyrrolic N, graphitic N, and oxidized N [78]. It was reported that the pyridinic N could alter the electronic distribution of adjacent carbon atoms thus facilitate the intermediate adsorption, while the graphitic N could improve the diffusion-limited properties [79]. Chou's group [80] reported a MOF-derived strategy (Figure 15(a)) to fabricate a self-standing Co@NC structure. The N species in the carbon shell were simply modulated through the calcination temperature. 10.88 at% of total N with the highest fraction of pyridinic and graphitic N was obtained under 700 °C (Figure 15(b)), which gave the catalyst the best ORR activity with an $E_{1/2}$ of 0.861 V (Figure 15(c)). A similar result was reported by Xing's group [81] in a Fe_3C@NC system. The optimal N doping was obtained under 800 °C (Figure 15(d)), enabling Fe_3C@NC an impressive durability in acidic solution with negligible degradation after 10,000 cycling (Figure 15(e)).

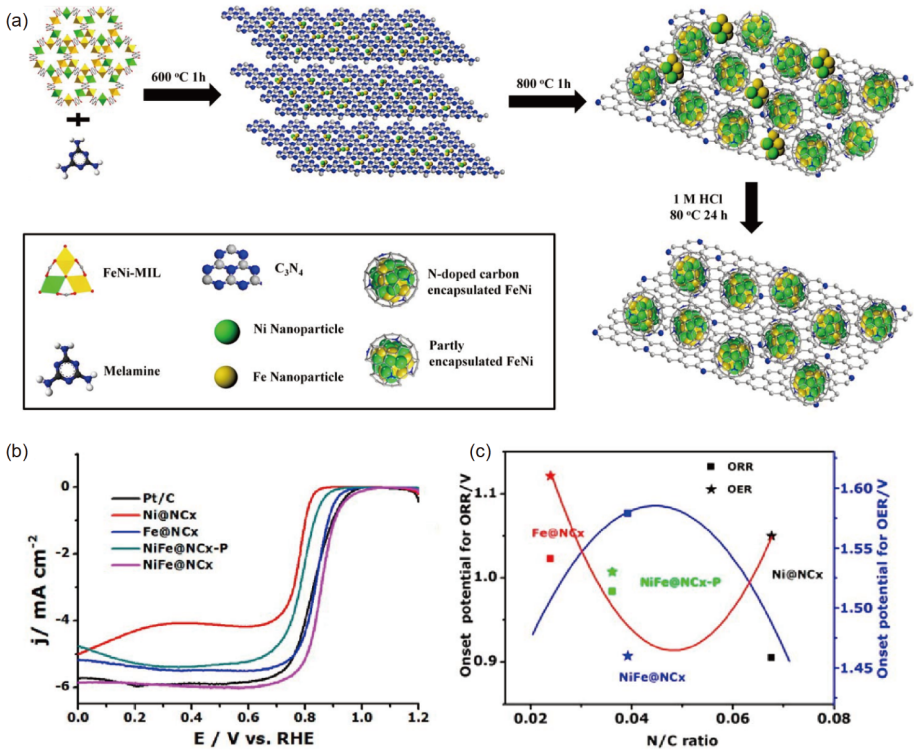

Figure 14 (a) Schematic synthesis of various M@NC$_x$ with single metal or bimetal cores *via* a two-stage MOF enabled strategy; (b) ORR curves and (c) the relationships between N/C ratio and ORR or OER onset potentials for various M@NC$_x$ catalysts. Adapted with permission from Ref. [75], Copyright by the American Chemical Society (color online).

4.3 Strategies to increase the density of M@NC active sites

4.3.1 Microporous polymer trapping strategy

To achieve a uniform and high-density distribution of nanoparticles, the substrate prefers to have strong interaction with metal species and could physically separate them. However, unmodified carbon-based materials usually have neutral surface and thus no abundant interaction sites for securing metal species [82]. Heteroatom-containing microporous polymer networks possess controllable pores to trap metal nanoparticles and π-conjugated structure for the strong interaction with them, offering opportunities for uniformly hosting high-density M@NC sites. Baek's group [83] reported a microporous polymer trapping strategy to prepare a Fe@NC structure. As illustrated in Figure 16, the reaction between 1,2,4,5-tetraaminobenzene (TAB) and hexaketocyclohexane (HKH) in the presence of iron (III) chloride ($FeCl_3$) was applied to form Fe^{3+}-sandwiched Aza-PON sheets. The built-in nitrogenated holey phenazine units in the Aza-PON structure provided abundant coordination sites to sequester Fe^{3+}. Theoretical calculations supported that the aromatic nitrogen in phenazine could effectively coordinate with the Fe_3O_4 intermediate [84], preventing the aggregation of final Fe@NC. The achieved Fe@Aza-PON displayed excellent and steady ORR performance. Based on a similar idea, a two-dimensional porous network rich in nitrogen was later proposed to host metal species by the same group [85]. It could effectively prevent the acid-leaching of metal ions during ORR, improving the stability of the catalyst. With the flexible structures, these porous organic polymers as precursors may provide possibility for constructing a variety of high-loading M@NC catalysts.

4.3.2 N-containing conductive polymer assisted strategy

The anchoring of metal species and N-doping are necessary for designing high-performance M@NC ORR catalysts. N-containing conductive polymers such as polyaniline and polypyrrole provide not only abundant N-sites for securing metal ions and doping but also highly conjugated units for improving the conductivity of the derived carbon materials. These features make them suitable for fabricating high-performance M@NC catalysts.

Zelenay's group [18] reported a polyaniline derived Fe-Co@NC structure with excellent performance and durability in PEMFC. The synthetic approach is displayed in Figure 17 (a). A short-chain aniline oligomer was first mixed with transition metal precursors and carbon supports, and then subject to pyrolysis, followed by acid-washing to remove the unstable species. The achieved FeCo nanoparticles were well protected by multiple graphitized carbon layers. Such a structure offered the catalyst outstanding durability in fuel

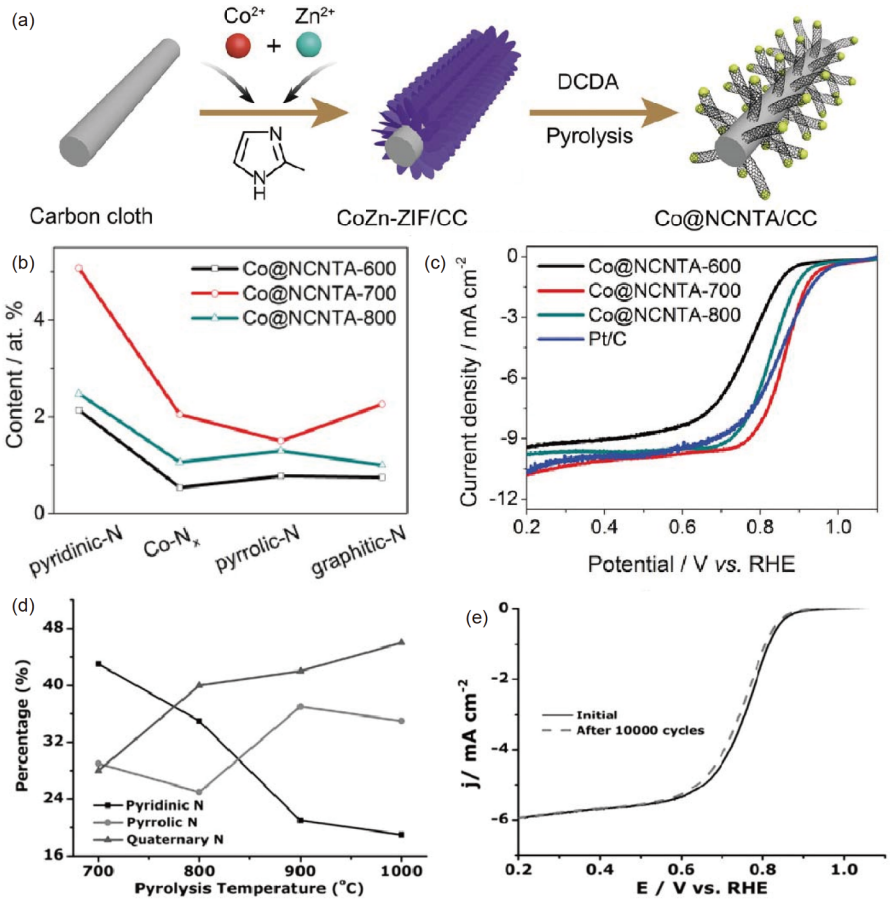

Figure 15 (a) Schematic synthesis of self-standing Co@NC; (b) Comparison of different N species in Co@NC under different calcine temperatures; (c) ORR curves of various Co@NC catalysts in 0.1 M KOH; (d) Percentages of N species in Fe_3C@NC prepared under various temperatures; (e) ORR curves of Fe_3C@NC before and after 10,000 cycles in 0.1 M $HClO_4$. Adapted with permission from Refs. [80,81], Copyright by Wiley, respectively (color online).

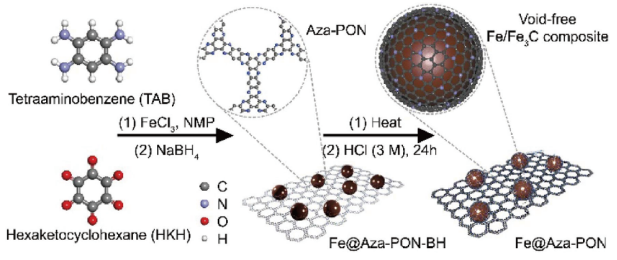

Figure 16 Schematic synthesis of Fe@NC using porous polymer Aza-PON as a precursor. Adapted with permission from Ref. [83], Copyright by the American Chemical Society (color online).

cell tests. The current density only declined by 3% after 700 h operation (Figure 17(b)). It was suggested that the onion-like graphitized carbon shells enhanced both electronic conductivity and corrosion resistance of the catalysts. Later on, they systematically investigated the effects of pyrolysis conditions, metal salts, and carbon supports on the catalyst morphologies and performances [86]. Wei's group [87] also investigated the relationship between the molecular structure of polyaniline and the performance of derived Fe@NC catalysts. The morphology of the polyaniline was controlled by the molar ratios of ammonium persulfate to aniline monomers. At a moderate ratio of 2.5, the achieved Fe@NC catalyst exhibited the best ORR activity.

Furthermore, other nitrogen-carbon precursors such as ethylenediamine, cyanamide, and dicyandiamide derived M@NC catalysts were also reported with high ORR performance [88–90]. These studies open up possibilities for the promising applications of M@NC catalysts in fuel cells.

4.3.3 *MOF derived M@NC*

MOFs have emerged as a new platform for the synthesis of M@NC due to their unique framework structures and tunable N-rich ligands. The uniform metal-organic coordination enables metal ions to be spatially isolated by organic ligands. Wang's group [91] used MOFs to prepare Co@NC sites encapsulated in N-doped CNT (NCNT) frameworks. The as-prepared hollow frameworks retained the well-defined morphology of ZIF-67 particle precursor while the shells were composed of hierarchically interconnected NCNTs grown by the catalysis of Co nanoparticles. The Co nanoparticles were encapsulated in NCNTs and protected by nanotubes. Benefiting from the synergistic effect from such

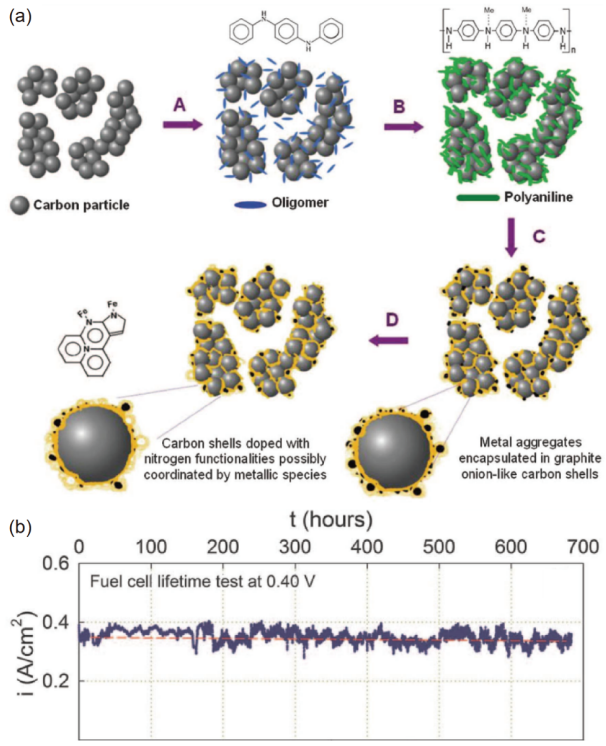

Figure 17 (a) Schematic synthesis of FeCo@NC catalysts through polyaniline; (b) long-term stability test of FeCo@NC at a constant fuel cell voltage of 0.40 V. Adapted with permission from Ref. [18], Copyright by the American Association for the Advancement of Science (color online).

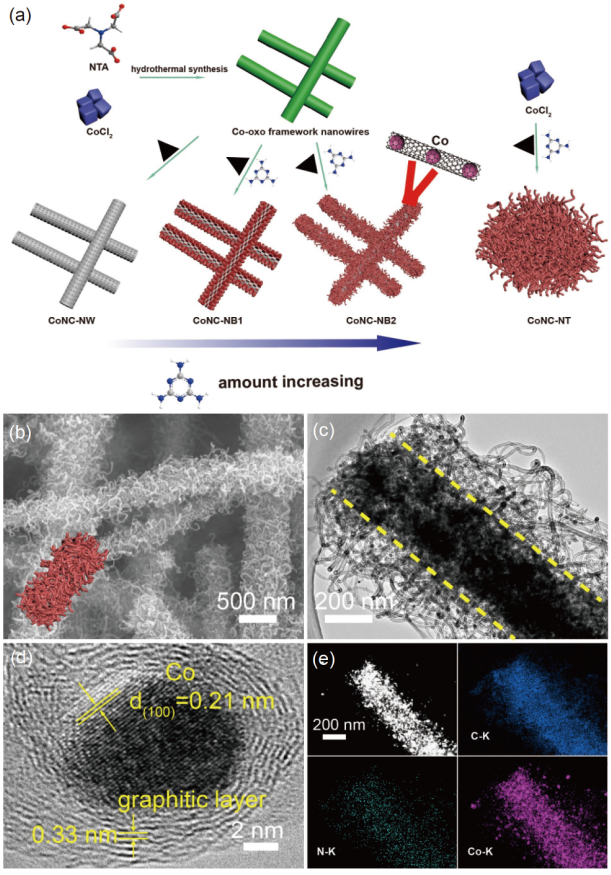

Figure 18 (a) Schematic preparation of various Co@NC nanostructures *via* MOF nanowire precursor; (b) SEM image, (c) TEM image, (d) HRTEM image, and (e) EDS elemental mapping images of CoNC-NB_2 in (a). Adapted with permission from Ref. [92], Copyright by Wiley (color online).

structure and the three-dimensional (3D) robust hollow framework, the catalyst exhibited enhanced ORR activity with an $E_{1/2}$ of 0.87 V and good stability.

Recently, we developed a scalable and facile self-catalyzed growth strategy for fabricating 3D brush-like Co@NC nanostructures using MOF nanowires as the precursor [92]. As shown in Figure 18(a), Co-oxo framework nanowire with uniform distribution of N, C, and Co at the molecular level was used as both precursor and backbone. During the pyrolysis, Co nanoparticles decomposed from Co-oxo frameworks catalyzed the growth of N-doped carbon nanotubes on the nanowire backbones with melamine as N and C source, giving Co@NC nanobrush-like structures. The morphology of the achieved nanobrushes could be easily adjusted by varying the amount of melamine during the pyrolysis. The best performed Co@NC catalysts exhibited a nanobrush morphology composed of Co@NC nanoparticles assembled nanowire backbones with Co, N-codoped carbon nanotube branches (Figure 18(b, c)). High resolution transmission electron microscopy (HRTEM) image taken on a single nanoparticle at the end of nanotube showed a well-defined Co@NC unit with a darker Co core protected by multiple graphitic carbon shells (Figure 18(d)). STEM image and corresponding energy dispersive X-ray spectroscopy (EDS) elemental mapping evidenced the homogenous distribution of C, N, and Co in the sample (Figure 18(e)). Systematic investigations suggested that the Co@NC nanobrushes delivered significantly improved electrocatalytic activity compared with Co@NC nanowire or pure nanotube counterparts, benefiting from the increase of accessible highly active sites and enhanced mass transfer and electron transportation. The nanobrushes with the longer nanotube branches presented better performance. Such a strategy could be extended to prepare other M@NC analogs, providing the opportunities for the application of MOF-derived nanobrush-like M@NC catalysts in the energy-related devices.

4.3.4 *Metastable rocksalt-oxide mediated strategy*

The catalyst performance in devices such as fuel cells or metal-air batteries is significantly affected by the charge transport and mass transfer. The high loading of active components in the catalyst is required for achieving high-performance devices. It cannot be fulfilled by simply raising catalyst loading since the thick catalyst layer would cause the mass/charge transfer issues [57]. Constructing high-density active sites is more practical [17]. Although many efforts have been made including the above-mentioned strategies, the agglomeration of metallic nanoparticles is nearly in-

evitable in high-temperature pyrolysis due to their highly reactive nature when the metal loading goes up. The resulting metal loading in M@NC with attractive performance is usually lower than 10 wt%, especially after acid leaching [75,93]. The controllable synthesis of high-density well-defined M@NC, especially well-protected by carbon layers, is still challenging.

Very recently, we discovered a metastable rocksalt oxide-mediated strategy. It was able to produce small-size, high-density, uniformly-distributed, and well-protected M@NC sites [94]. To avoid the uncontrollable thermal decomposition and inevitable aggregation of metal nanoparticles, pre-preparing well-dispersed precursors such as metal oxide nanoparticles on support instead of direct pyrolysis of metal sources would be an option for achieving the goal. Unfortunately, the thermal reduction of thermodynamically stable spinel metal oxides still led to the aggregation of metallic particles. Theoretical analyses indicated that the metastable rocksalt phase metal oxide had stronger interaction with graphene substrate compared with spinel phase counterparts, offering the opportunity for figuring this issue out. This inspired us to synthesize well-defined M@NC starting with fabricating high-density individual rocksalt oxide nanoparticles as intermediates from hydroxide nanosheet precursor. In a typical synthesis (Figure 19(a)), the hydroxide nanosheets were coated with an ultrathin polydopamine (PDA) layer as reductive carbon sources and additional protection layer, then subject to the controllable pyrolysis. Taking Co_2Fe_1 as an example, the well-dispersed metallic Co_2Fe_1 alloy nanoparticles completely encased in N-doped graphitic carbon shells (Co_2Fe_1@NC) (Figure 19(b)) were achieved by constructing CoFe hydroxide and thermally reducing *in-situ* generated rocksalt Co_2Fe_1 oxide intermediates. The PDA layer was simultaneously carbonized into a porous carbon network, anchoring these M@NC nanoparticles onto graphene support (Figure 19(c)). The phase and morphology transition during the whole process was monitored by systematic *in-situ* temperature-dependent electron microscopy and X-ray diffraction techniques, convincible evidencing the rocksalt oxide-mediated process. Combining with a series of control experiments, it was found that the rocksalt metal oxide intermediates were essential in achieving such a unique structure. For the typical Co_2Fe_1@NC, the nanoparticle size was centered at 15±5 nm. The metal loading of 54.0 wt% was easily obtained without further optimization. Importantly, every nanoparticle was entirely encapsulated by complete graphene-like N-doped carbon layers (Figure 19(d)), which were *in-situ* grown onto the nanoparticle, like the growth of graphene. Furthermore, all these M@NC nanoparticles were double armored by the outer porous carbon network derived from the carbonization of PDA coating and anchored onto the graphene substrate.

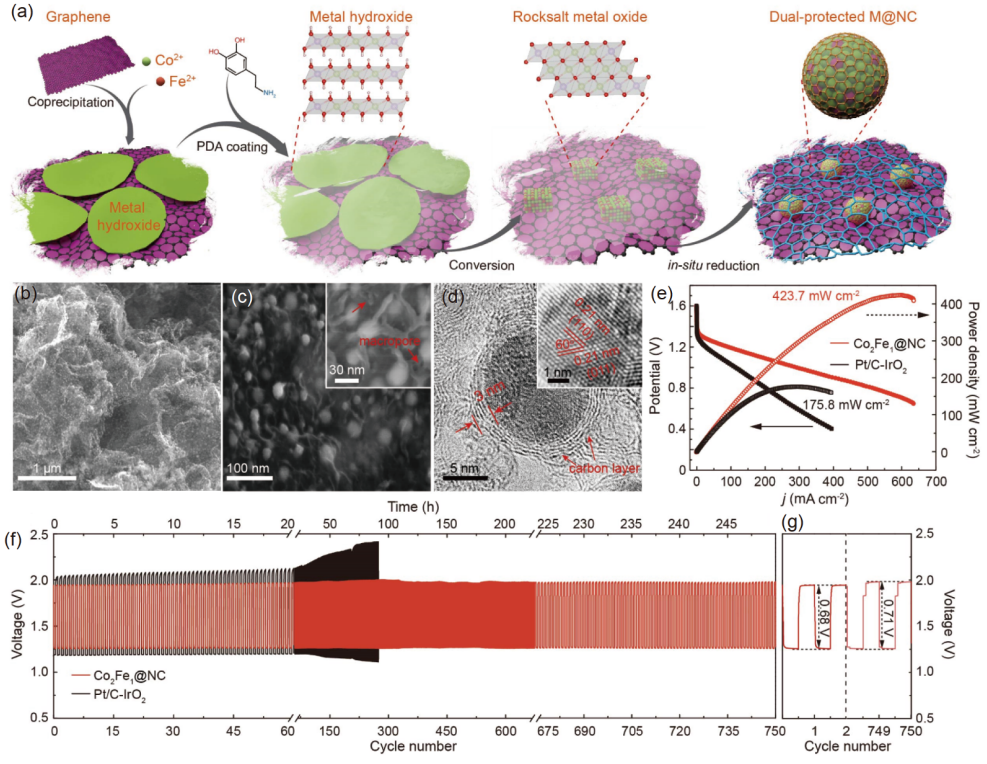

Figure 19 (a) Scheme for the synthesis of high-density well-dispersed Co_2Fe_1@NC *via* a rocksalt oxide-mediated strategy; (b) overview SEM image, (c) HRSEM image, and (d) HRTEM image of Co_2Fe_1@NC; (e) Zn-air performance and (f, g) long-time cycling of the devices with Co_2Fe_1@NC and Pt/C-IrO_2. Adapted with permission from Ref. [94], Copyright by the American Chemical Society (color online).

Such high-density well-protected M@NC sites promised the superior ORR and OER activity as well as remarkable durability, qualifying zinc-air batteries a record-high power density of 423.7 mW cm^{-2} (Figure 19(e)) and a long cycling life over 750 cycles (Figure 19(f, g)). This strategy may bring M@NC catalysts into the practical application of high-performance energy-related devices such as metal-air batteries and fuel cells.

5 Synergistic effects of M-N-C and M@NC

Although significant advancements have been achieved on the design and fabrication of well-defined M-N-C or M@NC ORR electrocatalysts, there are still a substantial amount of reported catalysts containing both of these two active sites. Some of them exhibit superior ORR performance. The understanding of the activity origin and the underlying catalytic mechanism for these catalysts are necessary to explore their practical applications.

We have systematically investigated and discovered that the metallic metal nanoparticles could significantly boost the ORR activity of the adjacent M-N_x sites (Figure 20(a)). Such a synergistic effect should be responsible for the high activity of M/N/C catalysts containing both sites [19,95]. To understand this effect, a series of catalysts containing only Fe-N-C sites (FeNC) or both Fe-N-C sites and Fe/Fe_3C nanocrystals wrapped in carbon layers (Fe@NC-FeNCs, two samples with various Fe-N_x content) were fabricated. The adjacent coexistence of Fe@NC and Fe-N-C sites was proved in Fe@C-FeNCs by EELS spectroscopy and EXAFS analyses. It was found that both Fe@NC-FeNCs showed the enhanced ORR activity compared with FeNC catalyst without Fe@NC sites in spite that the latter had a higher amount of Fe-N_x sites (Figure 20(b, c)). The control experiments indicated that the ORR activity appreciably decreased upon the removal of Fe@NC nanoparticles. These results suggested that Fe@NC played a critical role in enhancing activity. Moreover, comparing the two Fe@NC-FeNC samples with a similar structure, the ORR activity was positively correlated with the content of Fe-N_x sites. The poisoning experiments demonstrated that blocking Fe-N_x sites degraded the ORR activity while the release of the blocked Fe-N_x sites recovered the activity. These facts suggested that the ORR process should preferentially take place on the Fe-N_x site and the neighboring Fe@NC could boost its ORR activity. This finding was further rationalized by DFT calculation. It indicated that the interaction between metallic iron and Fe-N_4 sites favored the adsorption of oxygen molecules, thus promoting ORR on it.

Recently, we further investigated the influences of the metal chemical state in M@NC on this synergistic effect and ORR activity [95]. The iron porphyrins with various substituents were chosen as precursors to obtain Fe@FeNCs and Fe_3O_4@FeNCs (Figure 21(a)). The systematic experiments discovered that metallic Fe nanoparticles promoted the ORR

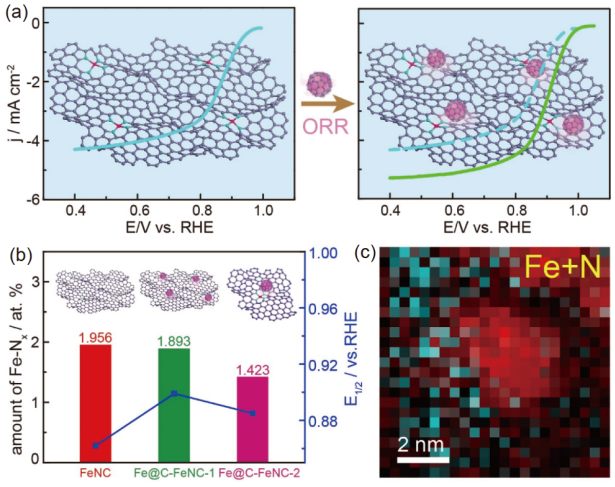

Figure 20 (a) Schematic for Fe@NC boosting the activity of Fe-N_x; (b) the correlation between the amount of Fe-N_x coordination and catalytic ORR performances for Fe@NC-FeNCs; (c) EELS mapping of Fe@C-FeNC-1. Adapted with permission from Ref. [19], Copyright by the American Chemical Society (color online).

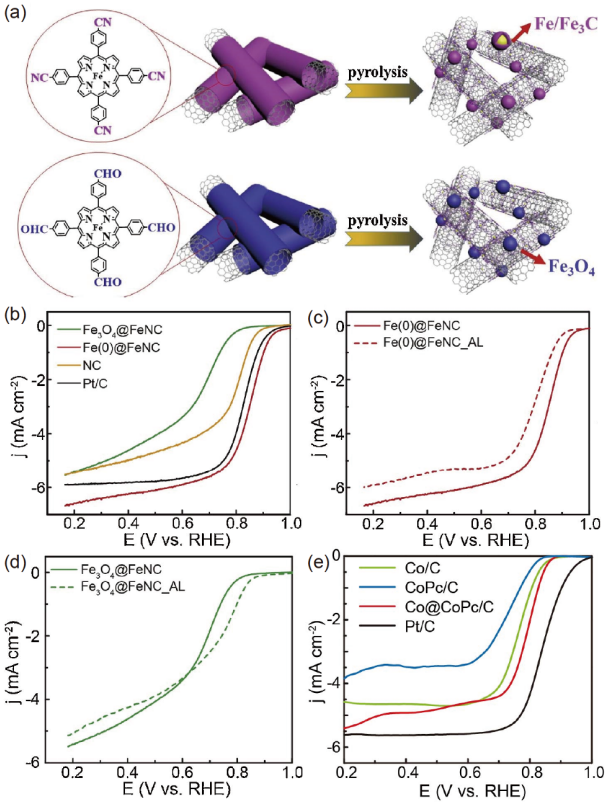

Figure 21 (a) Schematic preparation of Fe@FeNC and Fe_3O_4@FeNC. (b) ORR LSV curves of various catalysts. (c, d) ORR LSV curves of Fe@FeNC (c) and Fe_3O_4@FeNC (d) before and after acid leaching. Adapted with permission from Ref. [95], Copyright by Elsevier. (e) ORR LSV curves of Co/C, CoPc/C, Co@CoPc/C and Pt/C (color online).

on Fe-N_x sites while oxidative Fe_3O_4 nanoparticles inhibited the ORR (Figure 21(b)). The removal of metallic Fe@NC degraded the activity while the removal of Fe_3O_4@NC upgraded it (Figure 21(c, d)). These insights on the effect of chemical environments on the performance of M/N/C catalysts would shed light on the design of highly-efficient ORR catalysts.

To gain the unambiguous insight on the synergy of M-N-C and M@NC on ORR performance, we further designed model catalysts containing molecular cobalt phthalocyanine (CoPc) as well-defined Co-N_4 sites. It was noted that when integrating metallic Co nanoparticles with CoPc, the ORR activity was considerably boosted, compared with CoPc or Co nanoparticles itself (Figure 21(e)). In view of the clear-cut active sites, these molecular-level evidence directly supported that M@NC could promote the ORR process on M-N-C sites.

This synergistic effect can also be found in quite a lot of other similar catalysts. For example, as we mentioned in Section 4.3.2, Zelenay's group [18] reported polyaniline derived M@NC catalysts with FeCo nanoparticles encapsulated in carbon shells. It is reasonable to speculate that the two heat-treatment steps could create M-N_x sites although there was no direct characterization in the paper. The interaction of FeCo@NC and M-N_x sites might lead to the superior ORR activity of the catalyst. Yang's group [96] also reported a Co nanoparticle embedded in Co-N-C structure with synergistic enhanced ORR performance. They performed DFT calculations to prove that the introduction of Co nanoparticle optimized the binding energies of the reaction intermediates on Co-N-C site, thus enhanced the ORR performance. Such a structure exhibited excellent durability in fuel cell tests. Similar phenomena were also reported by Wei *et al*. [97]. It is reasonably believed that such synergistic effects between M-N_x and M@NC can boost the catalytic performance in various catalytic systems.

6 Catalyst engineering for device application

Different from the half-cell measurements on the disk electrode under ideal conditions, the practical devices usually experience various issues, like water flooding, oxygen diffusion, mass transfer, and H_2O_2 corrosion. The overall device performance is not only affected by the intrinsic activity of the active site and its density but also determined by the accessibility of active sites and the effectiveness of mass transfer and charge transport. Engineering the catalyst architecture and understanding the underlying fundamental science from the mechanistic level to the device-level will advance the application of catalysts in the devices and the development of high-performance practical devices. In the meantime, durability is another requisite for a practical device. Exploring solutions to prolong the service life of M/N/C catalysts shall advance their practical utilization.

6.1 Porosity engineering

In a fuel cell, the catalysts are commonly supported or attached on the electrode surface to achieve high current densities. The cathodic catalyst layer in PEMFC for non-precious-metal (NPM) catalysts is usually over 100 μm thick (~10 μm for commercialized Pt/C catalyst), bringing about the charge and mass transfer problems. Since the ORR happens at the three-phase interface, the pore structure of catalyst plays a key role in achieving efficient mass transport. For M/N/C based materials, the Fe-N_x active sites are commonly hosted in the micropores of carbon matrix [98]. However, the H^+ and O_2 have limited access to the active sites in such micropores in a small size (1–2 nm) [99]. Only the outer surface active sites (on the substrate surface or inside accessible pores) can participate in the reaction. Those buried inside dense carbon matrix and non-accessible pores stay inactive (Figure 22). Therefore, introducing macropores and mesopores into catalysts would benefit the exposure of such active sites as well as oxygen diffusion and mass transfer. Simply increasing the concentration of the active sites is not enough to boost the activity of carbon-based ORR catalysts. The rational design of catalyst porosity would advance its performance in the fuel cell operation.

Hyeon's group [100] recently investigated the effect of the pore structures on ORR performance. They prepared three Fe-N-C catalysts with similar Brunauer-Emmett-Teller (BET) surface areas and the number of active sites but significantly different pore structures: *i.e.*, mesopore-free, macropore-free and one with both types of pores (Figure 23(a)). The macropores come from the interspaces between prepared nanospheres with a diameter around 50–100 nm. It was found that the mesopores and macropores contributed to the different stages in reaction kinetics (Figure 23(b)). The mesopores benefited the electrolyte access to catalyst surface, increasing the amount of electrochemically available active sites. The macropores come from the interspaces

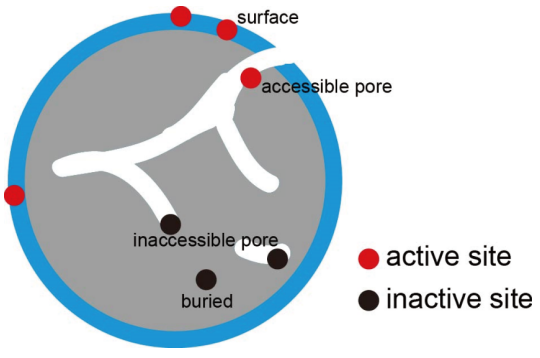

Figure 22 Schematic of the different types of active sites (color online).

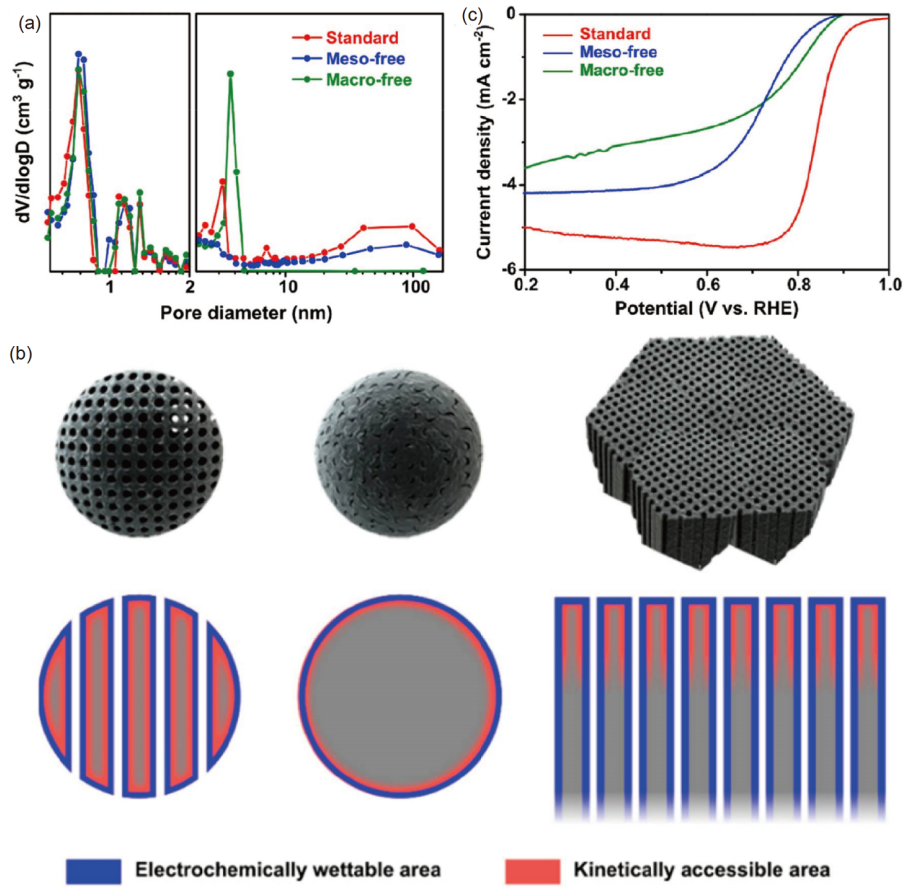

Figure 23 (a) Pore size distribution, (b) schematic illustration of electrochemically wettable and kinetically accessible area, and (c) ORR curves of three model catalysts with different porous structures. Adapted with permission from Ref. [100], Copyright by the American Chemical Society (color online).

greatly enhanced the mass transfer thus promoted the accessibility of reactant to active sites thus promoted kinetic accessibility to the available active sites. Without such macropores, the reactant could only reach the near-surface area of bulk catalysts, leading to poor kinetics. The catalyst with both mesopores and macropore thus exhibited a better ORR performance than the other two catalysts with one type of pores (Figure 23(c)).

The above results implied that a hierarchical porous structure with the multimodal pore size distribution of interconnected macro-, meso-, and micropores would be preferable to boost the accessibility of active sites. Zelenay's group [31] reported a catalyst with such hierarchical pore structures using double nitrogen-precursor (PANI and cyanamide (CM)). The catalyst had a surface area of ~1500 $m^2 g^{-1}$ with mesopore and micropore volumes of ~0.25 and ~0.61 $cm^3 g^{-1}$, respectively (Figure 24(a)). Such a large amount of micropores exposed high-density edge-hosted Fe-N_4 active sites, while the macropores provided the greater accessibility to these sites and established a more open framework for improving the ionomer distribution towards more three-phase interfaces. Such a hierarchical pore structure enabled the catalyst to significantly enhanced fuel cell performance. At the H_2-air condition (Figure 24(b)), the (CM+PANI)-Fe-C catalyst exhibited a similar current density to Pt/C catalyst in the kinetic region (>0.75 V). The peak power density of fuel cells thus reached 0.39 W cm^{-2}. At the H_2-O_2 condition, the peak power density even reached 0.94 W cm^{-2}. Such PEMFC performance indicated that the hierarchical porous structure effectively funneled the reactants and electrolytes into the active sites [101,102], critical for improving the ORR behavior of M/N/C based catalysts in the device.

As mentioned above, for M/N/C catalysts, not all Fe-N_x moieties can participate in the reaction. The micropore-hosted Fe-N_x moieties near the outer surface have more chances to involve in ORR, whereas the Fe species (Fe-N_x and/or Fe nanoparticles) buried in dense carbon matrix stay inactive. Creating mesopores as channels to make such sites accessible can increase the utilization of Fe-N_x moieties, thus the fuel cell performance. Shui's group [57] recently synthesized a concave-shaped Fe-N-C SACs (TPI@Z8(SiO_2)-650-C) with largely enhanced mesoporosity. As shown in Figure 25(a), the removal of the silica template resulted in a concave-shaped host with negative zeta potentials (ζ) and enlarged macropores for adsorbing Fe species. During the

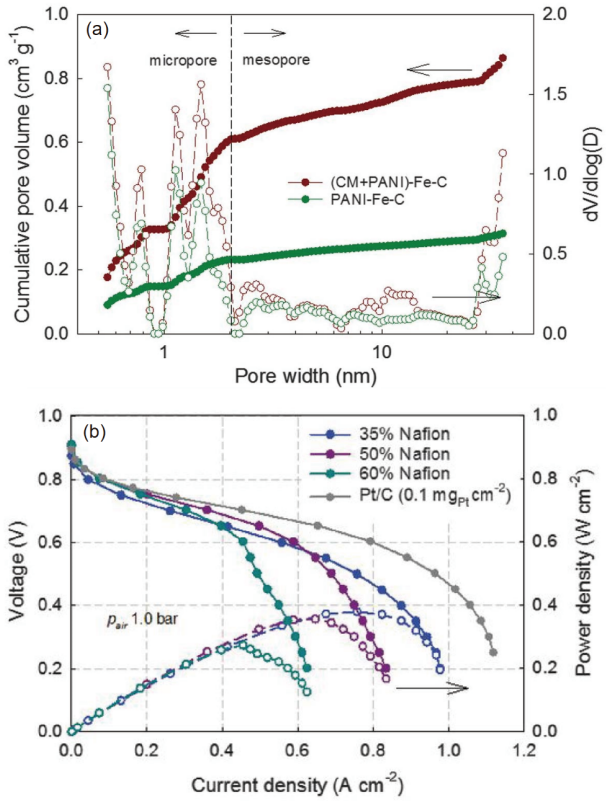

Figure 24 (a) Pore size distributions for (CM+PANI)-Fe-C and PANI-Fe-C; (b) H_2-air fuel cell polarization plots for the device with (CM+PANI)-Fe-C catalyst. Adapted with permission from Ref. [31], Copyright by the American Association for the Advancement of Science (color online).

pyrolysis, the adsorbed Fe species transformed into highly exposed Fe-N_x active sites sitting in the macropores, which could be easily accessed by the ionomer Nafion (Figure 25(b)) to create abundant three-phase interfaces for ORR. Besides, the existence of mesopores on the wall significantly increased the surface area. The concave architecture with abundant mesopores and a large external surface area (Figure 25(c)) was beneficial for boosting active site density and mass transport. As a result, in the H_2-O_2 fuel cell test (2.5 bar), the peak power density reached an impressive 1.18 W cm^{-2} (Figure 25(d)).

6.2 Strategies to improve device durability

Despite the promising activity of M-N-C catalyst in PEMFCs, the poor durability greatly limited their wide application [17,103]. The mechanistic understanding of the degradation process is urgently required and will advance the exploration of strategies for tackling this challenge. Generally speaking, the catalyst degradation involves two situations. As schematically shown in Figure 26(a), the fast demetallation commonly happens at below 0.7 V and the slow carbon corrosion takes place at above 0.9 V. Since the M/N/C catalysts are based on carbon materials, the electrochemical oxidation of carbon may cause the performance degradation in long term. Combining operando techniques with identical location-scanning transmission electron spectroscopy (IL-STEM), Mayrhofer *et al*. [103] identified that CO_2 evolution was detected at applied voltages higher than 0.9 V along with other oxidized functional groups such as COOH and –C=O. They demonstrated that such carbon corrosion not only led to the structural collapse of carbon materials but also drove the demetallation of M-N_x sites next to the oxidized carbon atoms. However, the fast demetallation that happens at the initial stage of PEMFC operation was generally considered as the dominate degradation mechanism for single-atomic M-N-C catalyst [104]. The kinetic dissolution of metal species could result from the inevitable protonation of neighboring N site as well as the chemical attack on metal site by H_2O_2 and radicals (Figure 26(b)) [103,105]. The dissolved metal ions such as Fe^{2+} could react with H_2O_2 to form Fe^{3+}, initiating serious Fenton reaction [106]. It would severely degrade the Nafion ionomer within the catalyst layer as well as the polymer membrane, thus causing further performance degradation. In this regard, Co- and Mn-based catalysts recently attract increasing attention due to their relatively low Fenton reaction activity [25,107]. Although the great progress has been made, the durability of M-N-C catalysts is still far from practical application in fuel cells. M@NC catalysts with metal nanoparticles well-encased by N-doped carbon shells and thus segregated from the corrosive environments showed enhanced durability in PEMFC operation, which may open up possibilities for the application. However, their performance requires further evaluation. The development of the suitable structures with both high activity and durability still remains a great challenge.

Recently, Liu's group [108] reported that the introduction of ultralow loading of Pt-Co alloy on the ZIF-derived Co-N/C catalyst synergistically enhanced the durability of PEMFC. As illustrated in Figure 27(a), Pt existed in form of CoPt alloy while the Co species existed in forms of both Co@NC and Co-N_x-C_y. The Pt-Co alloy increased oxygen utilization efficiency by not only catalyzing directly ORR but also facilitating the reduction of H_2O_2 generated from nearby Co/N sites, leading to the enhanced ORR activity as well as remarkable durability. Experimental results and DFT calculation indicated that the strong interaction of Pt surface with Co-N_4-C sites enhanced its binding energy on support, preventing the peel-off of Pt-Co nanoparticles. More importantly, as displayed in Figure 27(b), DFT calculations of ORR pathways on Pt surface and Co-N_4 site indicated that the reactions after step II* branched into two concurrent paths: the formation of O* and water (step III*) at Pt surface and the production of H_2O_2 (step IV*) on Co-N_4 site. Since H_2O_2 did not bind to the Co/N site, it could migrate to nearby Pt sites (as denoted by the green arrow in Figure 27(b)), then

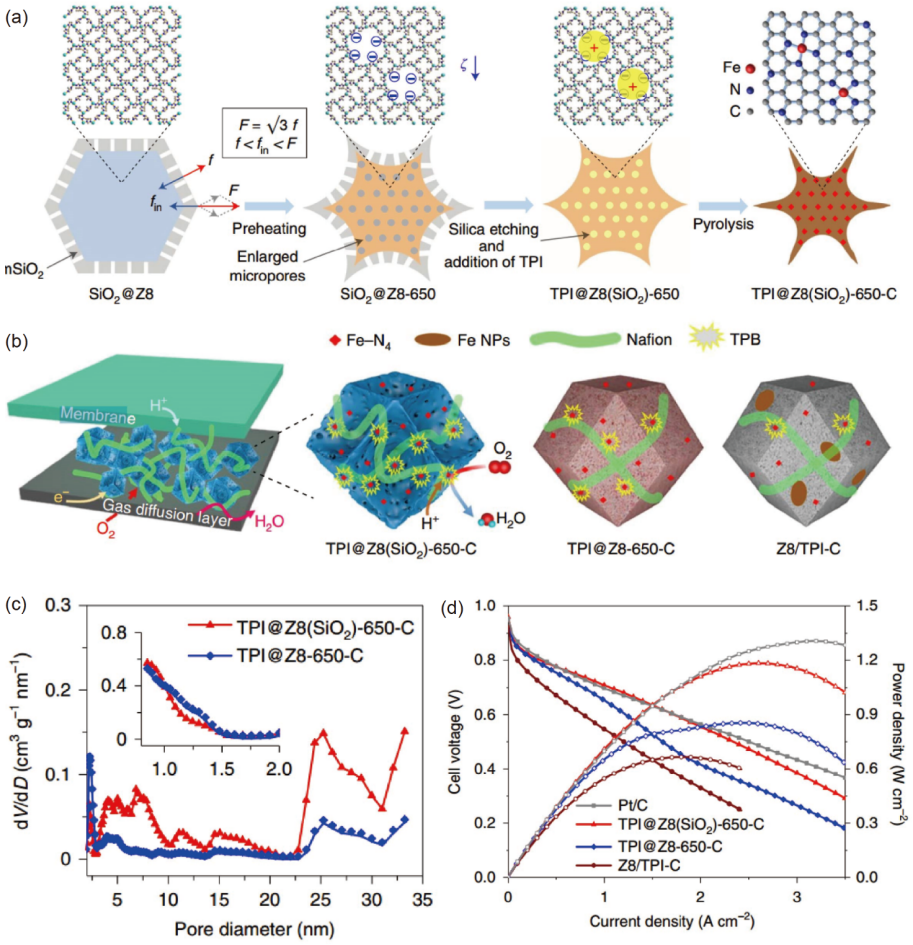

Figure 25 (a) Schematic synthesis of TPI@Z8(SiO_2)-650-C; (b) schematic TPB active sites in three representative Fe-N-C catalyst electrodes; (c) pore size distributions; (d) polarization and power density curves of the devices with the above catalysts. Adapted with permission from Ref. [57], Copyright by Nature publication group (color online).

fastly decomposed due to the nearly no thermodynamic barrier. This effect thus eliminated the corrosion of Co/N active sites by H_2O_2. Such synergistic interaction provided a possible solution to the durability problem of M/N/C based materials in fuel cell operation.

7 Low-cost scalable synthesis

Besides the efforts in designing highly-active catalysts and understanding the catalytic mechanism, the industrial application requires low-cost mass-production of M/N/C catalysts, calling for the consideration of cheap and abundant starting materials as well as the design of cost-effective, scalable, and manageable synthetic procedures.

For example, as mentioned above, we developed a feasible strategy for the mass-production of various M-N-C catalysts [24]. Experimentally, by simply dissolving cheap and readily-available glucose and metal salt together, then pyrolyzing the mixture, the target atomically-dispersed M-N-C catalysts were easily produced in gram-scale in one single batch in the laboratory (Figure 28). The whole process is ready to scale up and managed with no need for complex and expensive facilities, making the products cost-effective.

The green synthesis of catalysts with wastes such as biowastes is also attractive. We developed an effective strategy for directly turning biowastes such as animal blood in slaughter's house into Fe-N-C SAC through a simple pyrolysis process [109]. The hemoglobin cells containing molecular Fe-N_4 sites, rich in blood, enabled the formation of Fe-N-C SAC. Experimental results clearly evidenced the distribution of single-atomic Fe-N_x moieties in the pyrolyzed catalysts. By tuning the suitable pyrolysis temperature, the Fe-N-C catalyst could exhibit a high ORR activity with an $E_{1/2}$ of 0.851 V and a limited current density of 5.6 mA cm^{-2}. These results suggest that bio-enabled approaches could be used for the mass production of single-atomic M-N-C electrocatalysts.

Cost-effective processing is also required. Hard/soft templates such as SiO_2 or polymers have been used to alleviate the aggregation of metal species and achieve uniformly distributed active sites. However, these procedures require

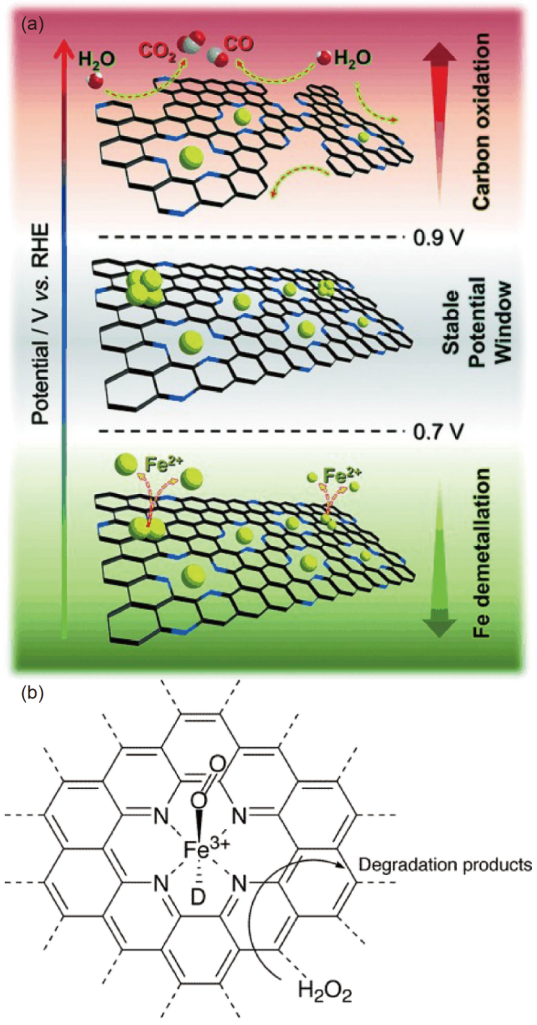

Figure 26 (a) Schematic deactivation paths of M-N-C under various electrochemical potential windows. Adapted with permission from Ref. [103], Copyright by Wiley. (b) Schematic of the demetallation of M-N-C structure. Adapted with permission from Ref. [105], Copyright by Elsevier (color online).

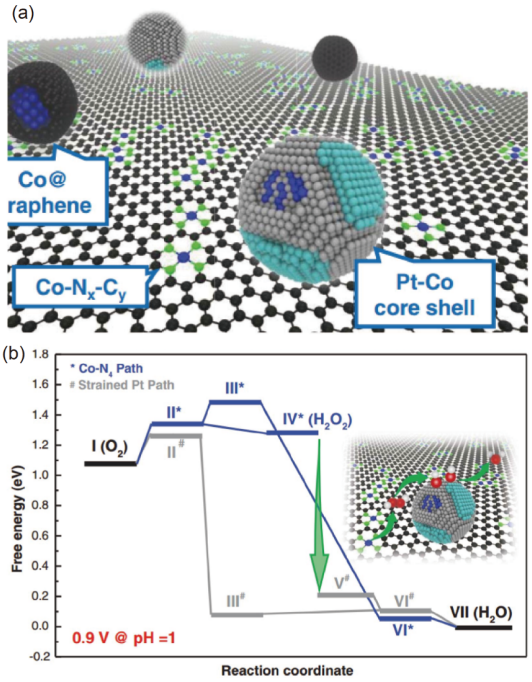

Figure 27 (a) Schematic of LP@PF catalysts; (b) free-energy diagram of the ORR pathways on LP@PF. Adapted with permission from Ref. [108], Copyright by the American Association for the Advancement of Science (color online).

additional processing and the removal of templates, leading to unscalable production and cost-ineffective catalysts. Moreover, the N species play a critical role in achieving active species for M/N/C catalysts. During the pyrolysis of N-containing carbon precursors, the substantial loss of N species is usually inevitable, leading to the lack of anchoring sites for securing metal atoms thus low-density active sites. We have developed a sodium chloride (NaCl) assisted green synthetic approach (Figure 29(a)) to fabricate 3D Fe/N/C hybrid catalysts [20]. The micrometer-scale NaCl crystallites were applied as recyclable skeletons to prevent the metal aggregation and increase the surface area of catalysts thus the number of active sites. It was not only cost-effective but also compatible with large-scale production. By just mixing NaCl, N, and C precursors together, followed by pyrolysis, the Fe/N/C catalysts with high-density Fe-N-C sites and Fe@NC active sites sitting on micrometer-sized graphitic carbon nanosheets connected with long CNTs were produced in quantity. NaCl crystallites effectively prevented the loss of nitrogen species and could be easily recycled for the next use. Compared with the conventional methods, this strategy provided higher N content and specific surface area while less material loss. Benefitting from the 3D hierarchical structure for improved mass/charge transfer and high-density active sites, the catalyst showed attractive ORR performance in terms of an $E_{1/2}$ of 0.869 V and excellent stability.

Similarly, Wei's group [110] reported a $ZnCl_2$/KCl eutectic salt assistant strategy to fabricate a hierarchically porous Fe/N/C catalyst. The semi-closed structure provided an ionic liquid-restricted space to reduce the vast loss of nitrogen precursor. The achieved Fe/N/C catalyst also exhibited superior ORR performance with $E_{1/2}$ of 0.803 and 0.918 V in acidic and basic media, respectively. A similar synthetic approach had also been applied by Li's group [111] to generate a series of M/N/C catalysts.

A majority of M/N/Cs are synthesized on the basis of solution processing, including dissolution, separation, and drying. The solid-state strategies are more facile and cost-effective over solution-based approaches in the matter of processing. As mentioned before, the gas-transport/migration approach is a scalable solid-state synthesis of M-N-C SACs [61]. We reported a green solid-state synthetic strategy ((Figure 29(b))) for the low-cost mass-production of M/N/C catalysts [112]. It only required one-step pyrolysis of a solid

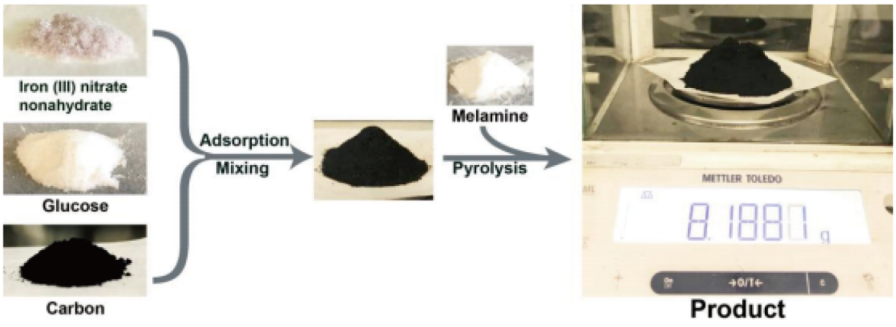

Figure 28 Scheme for a scale-up synthesis of Fe-NC SAC. Adapted with permission from Ref. [24], Copyright by Nature publication group (color online).

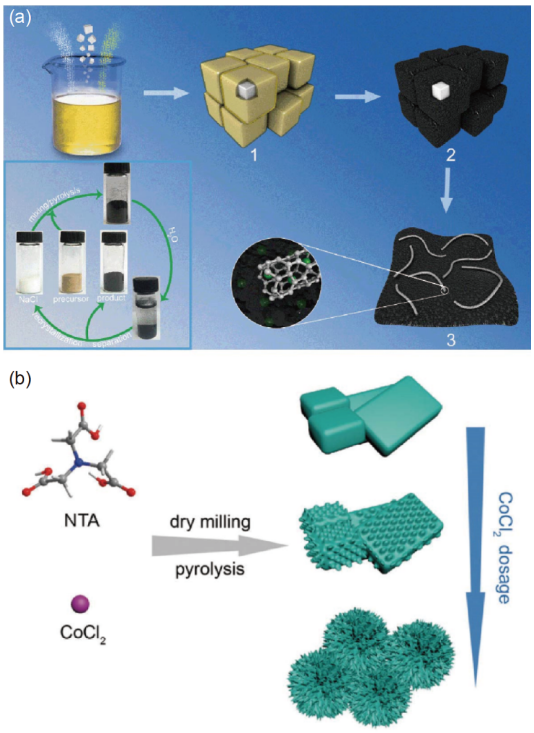

Figure 29 (a) Schematic production of 3D Fe/N/C hybrid catalysts; (b) schematic production of Co@CoNC. Adapted with permission from Refs. [20] and [112], Copyright by the Royal Society of Chemistry, respectively (color online).

mixture of cobalt chloride as the metal source and nitrilotriacetic acid as both carbon and nitrogen sources (Co@CoNC). The whole process was free of organic solvents and suitable for large-scale production. The morphology of as-prepared Co@CoNC could be regulated from aggregated bulk to a coralline-like 3D hierarchical structure by simply adjusting the dosage of $CoCl_2$. The optimal coralline-like morphology offered abundant active sites and enhanced mass/charge transport, leading to superior ORR performance. All the above-mentioned strategies provide opportunities for the mass production of highly-active M/N/C electrocatalysts for the potential industrial applications.

8 Summary and perspectives

The ultimate goal of the exploration of ORR catalysts is to achieve high-performance and durable devices such as fuel cells. Therefore, the design of M/N/C catalysts cannot only focus on constructing dense active sites with high intrinsic activity. The catalyst durability and its architecture specifically designed for device operation as well as the cost-effective scalable synthesis approach should also be considered (Figure 30). In this review, we have summarized the recent progress on two types of typical advanced M/N/C ORR electrocatalysts. Starting with understanding the activity origins of M-N-C and M@NC catalysts, we introduced the representative innovative strategies in enhancing the intrinsic activity and maximizing the active site density. In view of the substantial amount of reported catalysts containing both of these two active sites, we further discussed the synergistic effects of M-N-C and M@NC in enhancing the activity of catalysts. To achieve high-performance and durable devices, the recent structural engineering on M/N/C catalysts has also been introduced, aiming for exposing more accessible active sites and fast mass transport as well as extending service life. For practical application, the scale-up synthesis of M/N/C catalysts has lastly been discussed.

Although significant progress has been made in this field, there is still significant performance gap between current M/N/C catalysts and PGM-based catalysts [133]. As summarized in Table 1, the ORR activities in form of both on-set potential and half-wave potential as well as the power density in fuel cell tests for the state-of-the-art M/N/C catalysts are still appreciably lower than those of Pt-based counterparts in either acidic or alkaline media. The durability is even the bigger issue for the former, especially for the PEMFC application in acidic conditions.

In general, the M-N-C and M@NC structures have their own merits and drawbacks. For example, the M-N-C structures with $M\text{-}N_x$ active sites exhibit encouraging ORR performance in both half-cell measurements and PEMFCs. The peak power density around or even higher than 1 W cm^{-2} has

Table 1 Summary of state-of-the-art M/N/C and precious-metal catalyst ORR and fuel cell performance

Catalyst	Main active site type	E_{onset} (V)	$E_{1/2}$ (V)	P_{max} of fuel cell test (W cm^{-2})	Ref.
		Acidic media			
Pt/N-KB	Pt	–	~0.9	1.39	[113]
O-Pt_3Co NWs	Pt	–	0.928	1.22	[114]
$L1_0$-CoPt/Pt	Pt	–	0.967	–	[115]
$Pt_{75}Co_{25}$/C(500)	Pt	–	0.934	–	[116]
LP@PF-2	Pt+M-N-C (Co)	–	0.96	~1.41	[108]
Fe-N/P-C-700	M-N-C (Fe)	0.89	0.72	–	[50]
Fe-N_4/C	M-N-C (Fe)	0.8	~0.67	–	[51]
FeNC-S-MSUFC	M-N-C (Fe)	–	0.73	–	[53]
Fe-N-C-950	M-N-C (Fe)	0.92	0.78	–	[54]
(CM+PANI)-Fe-C	M-N-C (Fe)	–	0.8	0.94	[31]
ZIF-FA-CNT-p	M-N-C (Fe)	–	0.81	0.82	[117]
CNT/PC	M-N-C (Fe)	–	0.79	–	[65]
TPI@Z8(SiO_2)-650-C	M-N-C (Fe)	–	0.823	1.18	[57]
Fe-ZIF catalysts	M-N-C (Fe)	–	0.85	–	[118]
Fe/N/CF	M-N-C (Fe)	–	0.80	0.9	[119]
PFeTTPP-1000	M-N-C (Fe)	0.93	0.76	0.73	[120]
Fe/N/C-SCN	M-N-C (Fe)	–	0.836	1.03	[121]
Co-N-C@F127	M-N-C (Co)	–	0.84	0.87	[122]
Co-N-C	M-N-C (Co)	–	0.80	0.57	[123]
20Mn-NC-second	M-N-C (Mn)	–	0.8	0.46	[107]
PCN-FeCo/C	M-N-C (Fe, Co)	0.9	0.76	–	[124]
(Fe,Co)/N-C	M-N-C (Fe, Co)	1.06	0.863	0.98	[34]
(Fe,Mo)–N/C	M-N-C (Fe, Mo)	0.845	0.674	–	[125]
(Fe,Mn)-N-C-3HT-2AL	M-N-C (Fe, Mn)	0.92	0.82	–	[126]
Fe_3C/NG-800	M@NC (Fe)	0.92	0.77	–	[81]
Fe@Aza-PON	M@NC (Fe)	–	0.54	–	[83]
PANI-Fe-C	M@NC (Fe, Co)	0.91	0.81	0.55	[18]
Co@SACo-N-C-10	M@NC (Co)	0.92	0.778	0.42	[96]
ZIF-TAA-p	M@NC (Co)	0.9	0.78	–	[127]
Fe-NMCNF-800	M@NC (Fe)	0.59	0.51	–	[128]
LDH@ZIF-67-800	M@NC (Co)	0.875	0.675	–	[129]
		Alkaline media			
Pt/C	Pt	–	–	1	[130]
PdMo bimetallene/C	Pd	–	0.95	–	[131]
CNT/PC	M-N-C (Fe)	–	0.88	0.58	[65]
AT-Fe/N/C	M-N-C (Fe)	–	0.926	0.164	[132]
FeBNC-800	M-N-C (Fe)	0.968	0.838	–	[47]
Fe-N/P-C	M-N-C (Fe)	0.941	0.867	–	[50]
Fe-N_4/C	M-N-C (Fe)	0.95	0.837	–	[51]
$FeCl_1N_4$/CNS	M-N-C (Fe)	–	0.921V	–	[52]
Fe–NC SAC	M-N-C (Fe)	0.98	0.9	–	[24]
FeNC-900	M-N-C (Fe)	–	0.85	–	[109]
Co-N,B-CS	M-N-C (Co)	0.89	0.83	–	[48]
Co SAs/N-C(900)	M-N-C (Co)	0.982	0.881	–	[25]
Cu-SAs/N-C	M-N-C (Cu)	0.99	0.895	–	[61]
Cu ISAS/NC	M-N-C (Cu)	–	0.92	–	[62]
(Fe,Mn)-N-C-3HT-2AL	M-N-C (Fe, Mn)	0.98	0.90	–	[126]
Fe@C-FeNC	M@NC (Fe)	–	0.899	–	[19]
Fe/Fe_3C@N-C-NaCl	M@NC (Fe)	0.970	0.869	–	[20]
CoNC-NB_2	M@NC (Co)	1.04	0.88	–	[92]
NCNTFs	M@NC (Co)	–	0.87	–	[91]
Co@NCNTAs-700	M@NC (Co)	0.973	0.861	–	[80]
Co_2Fe_1@NC	M@NC (Fe, Co)	0.99	0.85	–	[94]
NiFe@NC_x	M@NC (Fe, Ni)	1.06	0.86	–	[75]
Fe_2Ni@NC	M@NC (Fe, Ni)	1.02	0.89	–	[76]

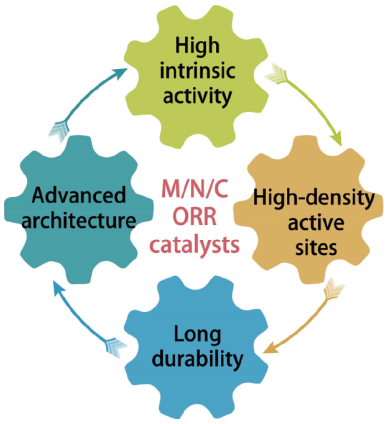

Figure 30 Four key objectives for advanced M/N/C ORR electrocatalysts (color online).

been reported in H_2-O_2 fuel cells, approaching conventional Pt/C catalysts. Unfortunately, the M-N-C sites are still very vulnerable in PEMFC applications, even for the state-of-the-art ones [105]. The limited durability of M-N-C catalysts is mainly due to the H_2O_2 attack or nearby N protonation *etc.*, leading to the irreversible metal loss [134]. In contrast, the M@NC structures show promising durability in the practical fuel cells. This is due to the shielding from the graphitic carbon shells, which secures the metal cores from the corrosive electrolyte. However, the intrinsic activity of such a structure is still inferior to M-N_x counterparts. The reported peak power density for M@NC-based PEMFC rarely reaches 0.5 W cm^{-2}, much less than M-N-C based ones. The efforts on raising the intrinsic activity and density of M@NC sites in a catalyst with the architecture optimized for device applications are still needed.

The future exploration of M/N/C catalysts for fuel cell applications will have to focus on both the catalytic activity and durability. Understanding the formation of catalytic sites and the catalytic mechanisms is still the foundation for addressing these issues. Although significant progress has been made recently, unveiling the nature of active sites *via* the emerging operando techniques still need to be paid more attention. These knowledges will ground the development of the innovative strategies for constructing well-defined highly-active and durable catalytic sites *via* designed precursors and/or synthetic routes.

Solving the durability issues for M-N-C catalysts is urgent for their applications in fuel cells. Fortunately, the rapid development of synthetic strategies offers opportunities to design stable and efficient M-N_x sites. Recent studies have shown that Mn-N_4 sites seem to be more stable than Fe-N_4 sites [107]. Bimetal (Fe, Co)/N-C sites also demonstrated the promising durability [34]. Combining active species to alleviate the production of H_2O_2 and/or the protonation of N species will also be effective to enhance the durability of M-N-C catalysts.

For relatively more stable but less-active M@NC catalysts, the in-depth mechanistic understanding of the activity origins will enable the design and construction of highly-active M@NC structures while keeping them well-protected is essential. The modification of metal cores and N species to favorably modulate the electronic structure of carbon shells might open up avenues to enhance their intrinsic activities.

One of the common challenges for both structures is that a majority of catalysts are currently prepared through the uncontrollable high-temperature pyrolysis. The achieved catalysts are usually heterogeneous in both active sites and distribution. Exploring new innovative strategies to massively produce high density structurally well-defined M-N-C and/or M@NC sites in uniform distribution would pave the way for achieving the qualified performance in devices and durability.

Last but not least, it is also critical to make the catalyst architecture suitable for water management, fast gas diffusion, and mass transport so as to meet the requirements for high-performance fuel cell devices. It is believed that with the unremitting efforts from the researchers worldwide, M/N/C catalysts will find their ways in their industrial applications in the near future.

Acknowledgements This work was supported by the National Key Research and Development Program of China (2016YFB0101202), and the National Natural Science Foundation of China (21773263, 21972147).

Conflict of interest The authors declare no conflict of interest.

1 Debe MK. *Nature*, 2012, 486: 43–51
2 Shao M, Chang Q, Dodelet JP, Chenitz R. *Chem Rev*, 2016, 116: 3594–3657
3 Liu J, Jin Z, Wang X, Ge J, Liu C, Xing W. *Sci China Chem*, 2019, 62: 669–683
4 Gewirth AA, Thorum MS. *Inorg Chem*, 2010, 49: 3557–3566
5 Kartha S, Grimes P. *Phys Today*, 1994, 47: 54–61
6 Proietti E, Jaouen F, Lefèvre M, Larouche N, Tian J, Herranz J, Dodelet JP. *Nat Commun*, 2011, 2: 416
7 Gewirth AA, Varnell JA, DiAscro AM. *Chem Rev*, 2018, 118: 2313–2339
8 Borghei M, Lehtonen J, Liu L, Rojas OJ. *Adv Mater*, 2018, 30: 1703691
9 Chen LN, Yu WS, Wang T, Yang XD, Yang HJ, Chen ZX, Wang T, Tian N, Zhou ZY, Sun SG. *Sci China Chem*, 2020, 63: 198–202
10 Hwang J, Noh SH, Han B. *Appl Surf Sci*, 2019, 471: 545–552
11 Jasinski R. *Nature*, 1964, 201: 1212–1213
12 Alt H, Binder H, Sandstede G. *J Catal*, 1973, 28: 8–19
13 Bagotzky VS, Tarasevich MR, Radyushkina KA, Levina OA, Andrusyova SI. *J Power Sources*, 1978, 2: 233–240
14 Gupta S, Tryk D, Bae I, Aldred W, Yeager E. *J Appl Electrochem*, 1989, 19: 19–27
15 Lim KH, Kim H. *Appl Catal B-Environ*, 2014, 158-159: 355–360
16 Cai P, Peng X, Huang J, Jia J, Hu X, Wen Z. *Sci China Chem*, 2019, 62: 385–392
17 Wang XX, Swihart MT, Wu G. *Nat Catal*, 2019, 2: 578–589
18 Wu G, More KL, Johnston CM, Zelenay P. *Science*, 2011, 332: 443–447
19 Jiang WJ, Gu L, Li L, Zhang Y, Zhang X, Zhang LJ, Wang JQ, Hu JS, Wei Z, Wan LJ. *J Am Chem Soc*, 2016, 138: 3570–3578

20 Zhang Y, Huang LB, Jiang WJ, Zhang X, Chen YY, Wei Z, Wan LJ, Hu JS. *J Mater Chem A*, 2016, 4: 7781–7787
21 Yang XF, Wang A, Qiao B, Li J, Liu J, Zhang T. *Acc Chem Res*, 2013, 46: 1740–1748
22 Li Z, Ji S, Liu Y, Cao X, Tian S, Chen Y, Niu Z, Li Y. *Chem Rev*, 2020, 120: 623–682
23 Zhang K, Guo W, Liang Z, Zou R. *Sci China Chem*, 2019, 62: 417–429
24 Zhao L, Zhang Y, Huang LB, Liu XZ, Zhang QH, He C, Wu ZY, Zhang LJ, Wu J, Yang W, Gu L, Hu JS, Wan LJ. *Nat Commun*, 2019, 10: 1278
25 Yin P, Yao T, Wu Y, Zheng L, Lin Y, Liu W, Ju H, Zhu J, Hong X, Deng Z, Zhou G, Wei S, Li Y. *Angew Chem Int Ed*, 2016, 55: 10800–10805
26 Han X, Ling X, Wang Y, Ma T, Zhong C, Hu W, Deng Y. *Angew Chem Int Ed*, 2019, 58: 5359–5364
27 Wang Q, Astruc D. *Chem Rev*, 2020, 120: 1438–1511
28 Qian Y, Khan IA, Zhao D. *Small*, 2017, 13: 1701143
29 Hao L, Zhang S, Liu R, Ning J, Zhang G, Zhi L. *Adv Mater*, 2015, 27: 3190–3195
30 Strickland K, Miner E, Jia Q, Tylus U, Ramaswamy N, Liang W, Sougrati MT, Jaouen F, Mukerjee S. *Nat Commun*, 2015, 6: 7343
31 Chung HT, Cullen DA, Higgins D, Sneed BT, Holby EF, More KL, Zelenay P. *Science*, 2017, 357: 479–484
32 Wu K, Chen X, Liu S, Pan Y, Cheong WC, Zhu W, Cao X, Shen R, Chen W, Luo J, Yan W, Zheng L, Chen Z, Wang D, Peng Q, Chen C, Li Y. *Nano Res*, 2018, 11: 6260–6269
33 Li Q, Chen W, Xiao H, Gong Y, Li Z, Zheng L, Zheng X, Yan W, Cheong WC, Shen R, Fu N, Gu L, Zhuang Z, Chen C, Wang D, Peng Q, Li J, Li Y. *Adv Mater*, 2018, 30: 1800588
34 Wang J, Huang Z, Liu W, Chang C, Tang H, Li Z, Chen W, Jia C, Yao T, Wei S, Wu Y, Li Y. *J Am Chem Soc*, 2017, 139: 17281–17284
35 Xiao M, Chen Y, Zhu J, Zhang H, Zhao X, Gao L, Wang X, Zhao J, Ge J, Jiang Z, Chen S, Liu C, Xing W. *J Am Chem Soc*, 2019, 141: 17763–17770
36 Sorokin AB. *Chem Rev*, 2013, 113: 8152–8191
37 Pegis ML, Wise CF, Martin DJ, Mayer JM. *Chem Rev*, 2018, 118: 2340–2391
38 Bettelheim A, Kuwana T. *Anal Chem*, 1979, 51: 2257–2260
39 Fang Y, Ou Z, Kadish KM. *Chem Rev*, 2017, 117: 3377–3419
40 Pegis ML, Martin DJ, Wise CF, Brezny AC, Johnson SI, Johnson LE, Kumar N, Raugei S, Mayer JM. *J Am Chem Soc*, 2019, 141: 8315–8326
41 Peng Y, Li Z, Xia D, Zheng L, Liao Y, Li K, Zuo X. *J Power Sources*, 2015, 291: 20–28
42 Chen Y, Ji S, Wang Y, Dong J, Chen W, Li Z, Shen R, Zheng L, Zhuang Z, Wang D, Li Y. *Angew Chem Int Ed*, 2017, 56: 6937–6941
43 Liu K, Wu G, Wang G. *J Phys Chem C*, 2017, 121: 11319–11324
44 Kneebone JL, Daifuku SL, Kehl JA, Wu G, Chung HT, Hu MY, Alp EE, More KL, Zelenay P, Holby EF, Neidig ML. *J Phys Chem C*, 2017, 121: 16283–16290
45 Jia Q, Ramaswamy N, Hafiz H, Tylus U, Strickland K, Wu G, Barbiellini B, Bansil A, Holby EF, Zelenay P, Mukerjee S. *ACS Nano*, 2015, 9: 12496–12505
46 Zhao Y, Wan J, Yao H, Zhang L, Lin K, Wang L, Yang N, Liu D, Song L, Zhu J, Gu L, Liu L, Zhao H, Li Y, Wang D. *Nat Chem*, 2018, 10: 924–931
47 Yuan K, Sfaelou S, Qiu M, Lützenkirchen-Hecht D, Zhuang X, Chen Y, Yuan C, Feng X, Scherf U. *ACS Energy Lett*, 2018, 3: 252–260
48 Guo Y, Yuan P, Zhang J, Hu Y, Amiinu IS, Wang X, Zhou J, Xia H, Song Z, Xu Q, Mu S. *ACS Nano*, 2018, 12: 1894–1901
49 Ma J, Xiang Z, Zhang J. *Sci China Chem*, 2018, 61: 592–597
50 Yuan K, Lützenkirchen-Hecht D, Li L, Shuai L, Li Y, Cao R, Qiu M, Zhuang X, Leung MKH, Chen Y, Scherf U. *J Am Chem Soc*, 2020, 142: 2404–2412
51 Ramaswamy N, Tylus U, Jia Q, Mukerjee S. *J Am Chem Soc*, 2013, 135: 15443–15449
52 Han Y, Wang Y, Xu R, Chen W, Zheng L, Han A, Zhu Y, Zhang J, Zhang H, Luo J, Chen C, Peng Q, Wang D, Li Y. *Energy Environ Sci*, 2018, 11: 2348–2352
53 Mun Y, Lee S, Kim K, Kim S, Lee S, Han JW, Lee J. *J Am Chem Soc*, 2019, 141: 6254–6262
54 Xiao M, Zhu J, Ma L, Jin Z, Ge J, Deng X, Hou Y, He Q, Li J, Jia Q, Mukerjee S, Yang R, Jiang Z, Su D, Liu C, Xing W. *ACS Catal*, 2018, 8: 2824–2832
55 Zagal JH, Koper MTM. *Angew Chem Int Ed*, 2016, 55: 14510–14521
56 Nørskov JK, Rossmeisl J, Logadottir A, Lindqvist L, Kitchin JR, Bligaard T, Jónsson H. *J Phys Chem B*, 2004, 108: 17886–17892
57 Wan X, Liu X, Li Y, Yu R, Zheng L, Yan W, Wang H, Xu M, Shui J. *Nat Catal*, 2019, 2: 259–268
58 Lee S, Kwak DH, Han SB, Lee YW, Lee JY, Choi IA, Park HS, Park JY, Park KW. *ACS Catal*, 2016, 6: 5095–5102
59 Lai Q, Zheng L, Liang Y, He J, Zhao J, Chen J. *ACS Catal*, 2017, 7: 1655–1663
60 Wang X, Fan X, Lin H, Fu H, Wang T, Zheng J, Li X. *RSC Adv*, 2016, 6: 37965–37973
61 Qu Y, Li Z, Chen W, Lin Y, Yuan T, Yang Z, Zhao C, Wang J, Zhao C, Wang X, Zhou F, Zhuang Z, Wu Y, Li Y. *Nat Catal*, 2018, 1: 781–786
62 Yang Z, Chen B, Chen W, Qu Y, Zhou F, Zhao C, Xu Q, Zhang Q, Duan X, Wu Y. *Nat Commun*, 2019, 10: 3734
63 Stariha S, Artyushkova K, Workman MJ, Serov A, Mckinney S, Halevi B, Atanassov P. *J Power Sources*, 2016, 326: 43–49
64 Monteverde Videla AHA, Osmieri L, Armandi M, Specchia S. *Electrochim Acta*, 2015, 177: 43–50
65 Sa YJ, Seo DJ, Woo J, Lim JT, Cheon JY, Yang SY, Lee JM, Kang D, Shin TJ, Shin HS, Jeong HY, Kim CS, Kim MG, Kim TY, Joo SH. *J Am Chem Soc*, 2016, 138: 15046–15056
66 You C, Zheng R, Shu T, Liu L, Liao S. *J Power Sources*, 2016, 324: 134–141
67 Wang Y, Kong A, Chen X, Lin Q, Feng P. *ACS Catal*, 2015, 5: 3887–3893
68 Eisenberg D, Stroek W, Geels NJ, Sandu CS, Heller A, Yan N, Rothenberg G. *Chem Eur J*, 2016, 22: 501–505
69 Niu W, Li L, Liu J, Wang N, Li W, Tang Z, Zhou W, Chen S. *Small*, 2016, 12: 1900–1908
70 Yang H, Shang L, Zhang Q, Shi R, Waterhouse GIN, Gu L, Zhang T. *Nat Commun*, 2019, 10: 4585
71 Pérez-Alonso FJ, Domínguez C, Al-Thabaiti SA, Al-Youbi AO, Abdel Salam M, Alshehri AA, Retuerto M, Peña MA, Rojas S. *J Power Sources*, 2016, 327: 204-211
72 Zhang Y, Jiang WJ, Guo L, Zhang X, Hu JS, Wei Z, Wan LJ. *ACS Appl Mater Interfaces*, 2015, 7: 11508–11515
73 Jia Q, Ramaswamy N, Tylus U, Strickland K, Li J, Serov A, Artyushkova K, Atanassov P, Anibal J, Gumeci C, Barton SC, Sougrati MT, Jaouen F, Halevi B, Mukerjee S. *Nano Energy*, 2016, 29: 65–82
74 Deng D, Yu L, Chen X, Wang G, Jin L, Pan X, Deng J, Sun G, Bao X. *Angew Chem Int Ed*, 2013, 52: 371–375
75 Zhu J, Xiao M, Zhang Y, Jin Z, Peng Z, Liu C, Chen S, Ge J, Xing W. *ACS Catal*, 2016, 6: 6335–6342
76 Zhu J, Xiao M, Li G, Li S, Zhang J, Liu G, Ma L, Wu T, Lu J, Yu A, Su D, Jin H, Wang S, Chen Z. *Adv Energy Mater*, 2020, 10: 1903003
77 Gong K, Du F, Xia Z, Durstock M, Dai L. *Science*, 2009, 323: 760–764
78 Zhang J, Xia Z, Dai L. *Sci Adv*, 2015, 1: e1500564
79 Guo D, Shibuya R, Akiba C, Saji S, Kondo T, Nakamura J. *Science*, 2016, 351: 361–365
80 Liu L, Wang Y, Yan F, Zhu C, Geng B, Chen Y, Chou S. *Small Methods*, 2020, 4: 1900571
81 Xiao M, Zhu J, Feng L, Liu C, Xing W. *Adv Mater*, 2015, 27: 2521–2527
82 Huo L, Liu B, Zhang G, Si R, Liu J, Zhang J. *J Mater Chem A*, 2017, 5: 4868–4878
83 Kim SJ, Mahmood J, Kim C, Han GF, Kim SW, Jung SM, Zhu G, De

Yoreo JJ, Kim G, Baek JB. *J Am Chem Soc*, 2018, 140: 1737–1742
84 Merzoug M, Zouchoune B. *J Organomet Chem*, 2014, 770: 69–78
85 Mahmood J, Li F, Kim C, Choi HJ, Gwon O, Jung SM, Seo JM, Cho SJ, Ju YW, Jeong HY, Kim G, Baek JB. *Nano Energy*, 2018, 44: 304–310
86 Wu G, Johnston CM, Mack NH, Artyushkova K, Ferrandon M, Nelson M, Lezama-Pacheco JS, Conradson SD, More KL, Myers DJ, Zelenay P. *J Mater Chem*, 2011, 21: 11392–11405
87 He Q, Chen X, Jia F, Ding W, Zhou Y, Wang J, Song X, Jiang J, Liao Q, Li J, Wei Z. *ChemistrySelect*, 2019, 4: 8135–8141
88 Wang X, Li Q, Pan H, Lin Y, Ke Y, Sheng H, Swihart MT, Wu G. *Nanoscale*, 2015, 7: 20290–20298
89 Kim BJ, Lee DU, Wu J, Higgins D, Yu A, Chen Z. *J Phys Chem C*, 2013, 117: 26501–26508
90 Wu G, Zelenay P. *Acc Chem Res*, 2013, 46: 1878–1889
91 Xia BY, Yan Y, Li N, Wu HB, Lou XWD, Wang X. *Nat Energy*, 2016, 1: 15006
92 Luo H, Jiang WJ, Niu S, Zhang X, Zhang Y, Yuan LP, He C, Hu JS. *Small*, 2020, 16: 2001171
93 Fan X, Peng Z, Ye R, Zhou H, Guo X. *ACS Nano*, 2015, 9: 7407–7418
94 Tang T, Jiang WJ, Liu XZ, Deng J, Niu S, Wang B, Jin SF, Zhang Q, Gu L, Hu JS, Wan LJ. *J Am Chem Soc*, 2020, 142: 7116–7127
95 Li Z, Wei L, Jiang WJ, Hu Z, Luo H, Zhao W, Xu T, Wu W, Wu M, Hu JS. *Appl Catal B*, 2019, 251: 240–246
96 Cheng Q, Han S, Mao K, Chen C, Yang L, Zou Z, Gu M, Hu Z, Yang H. *Nano Energy*, 2018, 52: 485–493
97 Wan X, Wu R, Deng J, Nie Y, Chen S, Ding W, Huang X, Wei Z. *J Mater Chem A*, 2018, 6: 3386–3390
98 Jaouen F, Lefèvre M, Dodelet JP, Cai M. *J Phys Chem B*, 2006, 110: 5553–5558
99 Yarlagadda V, Carpenter MK, Moylan TE, Kukreja RS, Koestner R, Gu W, Thompson L, Kongkanand A. *ACS Energy Lett*, 2018, 3: 618–621
100 Lee SH, Kim J, Chung DY, Yoo JM, Lee HS, Kim MJ, Mun BS, Kwon SG, Sung YE, Hyeon T. *J Am Chem Soc*, 2019, 141: 2035–2045
101 Sun G, Wang J, Liu X, Long D, Qiao W, Ling L. *J Phys Chem C*, 2010, 114: 18745–18751
102 Wang G, Sun Y, Li D, Liang HW, Dong R, Feng X, Müllen K. *Angew Chem Int Ed*, 2015, 54: 15191–15196
103 Choi CH, Baldizzone C, Grote JP, Schuppert AK, Jaouen F, Mayrhofer KJJ. *Angew Chem Int Ed*, 2015, 54: 12753–12757
104 Chenitz R, Kramm UI, Lefèvre M, Glibin V, Zhang G, Sun S, Dodelet JP. *Energy Environ Sci*, 2018, 11: 365–382
105 Banham D, Ye S, Pei K, Ozaki J, Kishimoto T, Imashiro Y. *J Power Sources*, 2015, 285: 334–348
106 Goellner V, Baldizzone C, Schuppert A, Sougrati MT, Mayrhofer K, Jaouen F. *Phys Chem Chem Phys*, 2014, 16: 18454–18462
107 Li J, Chen M, Cullen DA, Hwang S, Wang M, Li B, Liu K, Karakalos S, Lucero M, Zhang H, Lei C, Xu H, Sterbinsky GE, Feng Z, Su D, More KL, Wang G, Wang Z, Wu G. *Nat Catal*, 2018, 1: 935–945
108 Chong L, Wen J, Kubal J, Sen FG, Zou J, Greeley J, Chan M, Barkholtz H, Ding W, Liu DJ. *Science*, 2018, 362: 1276–1281
109 Jiang WJ, Hu WL, Zhang QH, Zhao TT, Luo H, Zhang X, Gu L, Hu JS, Wan LJ. *Chem Commun*, 2018, 54: 1307–1310
110 Li J, Chen S, Li W, Wu R, Ibraheem S, Li J, Ding W, Li L, Wei Z. *J Mater Chem A*, 2018, 6: 15504–15509
111 Zhang X, Zhang S, Yang Y, Wang L, Mu Z, Zhu H, Zhu X, Xing H, Xia H, Huang B, Li J, Guo S, Wang E. *Adv Mater*, 2020, 32: 1906905
112 Luo H, Jiang WJ, Lin C, Dong W, Niu S, Huang LB, Zhang X, Wei Z, Hu JS. *Chem Commun*, 2018, 54: 8190–8193
113 Ott S, Orfanidi A, Schmies H, Anke B, Nong HN, Hübner J, Gernert U, Gliech M, Lerch M, Strasser P. *Nat Mater*, 2020, 19: 77–85
114 Kim HY, Kim JM, Ha Y, Woo J, Byun A, Shin TJ, Park KH, Jeong HY, Kim H, Kim JY, Joo SH. *ACS Catal*, 2019, 9: 11242–11254
115 Li J, Sharma S, Liu X, Pan YT, Spendelow JS, Chi M, Jia Y, Zhang P, Cullen DA, Xi Z, Lin H, Yin Z, Shen B, Muzzio M, Yu C, Kim YS, Peterson AA, More KL, Zhu H, Sun S. *Joule*, 2019, 3: 124–135
116 Choi DS, Robertson AW, Warner JH, Kim SO, Kim H. *Adv Mater*, 2016, 28: 7115–7122
117 Zhang J, Liu X, Neri G, Pinna N. *Adv Mater*, 2016, 28: 795–831
118 Zhang H, Hwang S, Wang M, Feng Z, Karakalos S, Luo L, Qiao Z, Xie X, Wang C, Su D, Shao Y, Wu G. *J Am Chem Soc*, 2017, 139: 14143–14149
119 Shui J, Chen C, Grabstanowicz L, Zhao D, Liu DJ. *Proc Natl Acad Sci USA*, 2015, 112: 10629–10634
120 Yuan S, Shui JL, Grabstanowicz L, Chen C, Commet S, Reprogle B, Xu T, Yu L, Liu DJ. *Angew Chem Int Ed*, 2013, 52: 8349–8353
121 Wang YC, Lai YJ, Song L, Zhou ZY, Liu JG, Wang Q, Yang XD, Chen C, Shi W, Zheng YP, Rauf M, Sun SG. *Angew Chem Int Ed*, 2015, 54: 9907–9910
122 He Y, Hwang S, Cullen DA, Uddin MA, Langhorst L, Li B, Karakalos S, Kropf AJ, Wegener EC, Sokolowski J, Chen M, Myers D, Su D, More KL, Wang G, Litster S, Wu G. *Energy Environ Sci*, 2019, 12: 250–260
123 Wang XX, Cullen DA, Pan YT, Hwang S, Wang M, Feng Z, Wang J, Engelhard MH, Zhang H, He Y, Shao Y, Su D, More KL, Spendelow JS, Wu G. *Adv Mater*, 2018, 30: 1706758
124 Lin Q, Bu X, Kong A, Mao C, Bu F, Feng P. *Adv Mater*, 2015, 27: 3431–3436
125 Lin L, Yang ZK, Jiang YF, Xu AW. *ACS Catal*, 2016, 6: 4449–4454
126 Sahraie NR, Kramm UI, Steinberg J, Zhang Y, Thomas A, Reier T, Paraknowitsch JP, Strasser P. *Nat Commun*, 2015, 6: 8618
127 Zhang C, An B, Yang L, Wu B, Shi W, Wang YC, Long LS, Wang C, Lin W. *J Mater Chem A*, 2016, 4: 4457–4463
128 An GH, Lee EH, Ahn HJ. *J Alloys Compd*, 2016, 682: 746–752
129 Li Z, Shao M, Zhou L, Zhang R, Zhang C, Wei M, Evans DG, Duan X. *Adv Mater*, 2016, 28: 2337–2344
130 Wang Y, Yang Y, Jia S, Wang X, Lyu K, Peng Y, Zheng H, Wei X, Ren H, Xiao L, Wang J, Muller DA, Abruña HD, Hwang BJ, Lu J, Zhuang L. *Nat Commun*, 2019, 10: 1506
131 Luo M, Zhao Z, Zhang Y, Sun Y, Xing Y, Lv F, Yang Y, Zhang X, Hwang S, Qin Y, Ma JY, Lin F, Su D, Lu G, Guo S. *Nature*, 2019, 574: 81–85
132 Chen C, Yang XD, Zhou ZY, Lai YJ, Rauf M, Wang Y, Pan J, Zhuang L, Wang Q, Wang YC, Tian N, Zhang XS, Sun SG. *Chem Commun*, 2015, 51: 17092–17095
133 Li X, Zhang C, Du C, Zhuang Z, Zheng F, Li P, Zhang Z, Chen W. *Sci China Chem*, 2019, 62: 378–384
134 Ferrandon M, Wang X, Kropf AJ, Myers DJ, Wu G, Johnston CM, Zelenay P. *Electrochim Acta*, 2013, 110: 282–291